Correspondence to:

M. Ali and A. Decarlis,
momen.mohamed@science.au.edu.eg;
alessandro.decarlis@ku.ac.ae

Geophysical Evidence for Magmatism Southwest of the Brothers Islands, Northern Red Sea (Offshore Quseir, Egypt)

Moamen Ali[1,2,3] , **Marco Ligi**[4] , **Andrea Ceriani**[1,2], **Fateh Bouchaala**[1], **William Bosworth**[5], and **Alessandro Decarlis**[1,2]

[1]R.I.C.H. Center: Research and Innovation on CO₂ and H₂, Khalifa University of Science and Technology, Abu Dhabi, UAE, [2]Earth Sciences Department, Khalifa University of Science and Technology, Abu Dhabi, UAE, [3]Department of Geology, Assiut University, Assiut, Egypt, [4]Istituto di Scienze Marine, CNR, Bologna, Italy, [5]Apache Egypt Companies, Cairo, Egypt

Abstract The Red Sea formed as a consequence of Cenozoic rifting between the African and Arabian plates. While continuous oceanic spreading is active in the southern and central sectors, in the northern Red Sea, exposure of oceanic crust is limited to a few along-axis isolated deeps. However, several off-axis magmatic edifices have been recognized in this sector, their description in terms of relative age and architectural features remains vague. One of these, offshore Quseir corresponding to a kilometer-size structural high, was studied in detail using 3D industrial seismic data. This structure is interpreted as due to the coalescence of different volcanic edifices developed on the footwall of a major rift-related normal fault. Magnetic and gravity data and forward modeling suggest a volcanic nature of the substratum underlying the morphological relief. A similar volcanic origin is proposed for other neighboring basement hills that show a similar magnetic signal. Relationships with the imaged seismo-stratigraphic sequences point to a Pleistocene age for the magmatic event. Arabian alkali-basalts, at the same latitude as Quseir, show ages comparable to those inferred for the volcano edifice studied, suggesting a similar geotectonic context. In western Arabian plate, large alkali-lava fields (*Harrats*) developed along rift-related faults since the early stages of the Red Sea rift (Late Oligocene). They display a significant northward rejuvenation trend that may be explained by the progressive propagation of the Afar mantle plume.

1. Introduction

The Red Sea formed due to the separation of Arabia from Nubia during the Late Oligocene-Early Miocene, involving a counter-clockwise rotation of the Arabian plate. Although the southern and central sectors of the Red Sea reached the oceanic stage and display a prominent NW-SE oriented axial ridge, the nature of the crust in its northward termination is still controversial (e.g., Augustin et al., 2021). Onshore observations in the present-day margins of the northern Red Sea (NRS) indicate a "classic" rifted margin dynamic dominated by normal fault and half-graben geometries and provide constraints on the timing and evolution of rifting (Figure 1a; Bosworth & Burke, 2005; Cochran, 1983, 2005). Omar and Steckler (1995) concluded that the early stage of rifting was accompanied by two uplift and erosion phases of the shoulders. The first stage started ~34 Ma in the Early Oligocene, while the second uplift and erosion phase occurred during the latest Oligocene to Early Miocene. However, geological and thermochronometric evidence from the Quseir area on the Red Sea coast indicates that only the second uplift and erosion phase at 23 Ma exists (Bojar et al., 2002; Bosworth et al., 2005; Patton et al., 1994; Stockli & Bosworth, 2019). This uplift was accompanied by extension along the entire NRS, which hosted a significant and widespread syn-rift sequence (Bosworth & Burke, 2005; Jarrige et al., 1990; Montenat et al., 1988; Omar & Steckler, 1995). In addition, based on offshore exploration wells, some information on NRS stratigraphy is available (Hughes & Beydoun, 1992; Hughes & Johnson, 2005; Izzeldin, 1987). The rare outcrops observed at specific distal structural highs, such as Zabargad and Brothers Islands (Bonatti & Seyler, 1987), expose mantle and lower crustal rocks, leading some authors to consider the NRS rift as dominated by exhumation processes (Bosworth & Stockli, 2016; Ligi et al., 2018). Several works revealed the existence of recent magmatism forming large volcanic buildups in the Egyptian and Saudi margins (Ali et al., 2021; Ali, Ligi, et al., 2022; Augustin et al., 2019; Bosworth & Stockli, 2016; Cochran & Karner, 2007; Duncan & Al-Amri, 2013; Sanfilippo et al., 2021). Eighteen volcanic edifices have been recognized using magnetic and gravity anomalies in the NRS where the volcanoes formed after exhumation of the lower crust, and their age is supposed to be <14 Ma (Ball et al., 2018). Nevertheless, volcanism description in terms of age and geometry of the edifices remains vague.

In this paper, different geophysical data sets and techniques are used to suggest the possible occurrence of volcanic edifices offshore Quseir (Egypt) better to define the size and geometry of such magmatic outpourings and possibly more tightly constrain their age of formation. The regional implications of these findings and their significance related to NRS rift evolution are also addressed.
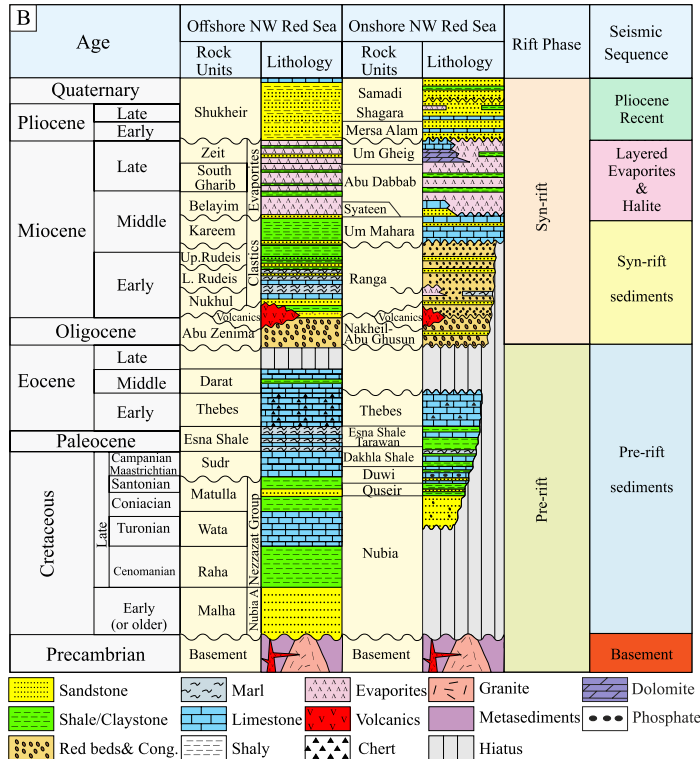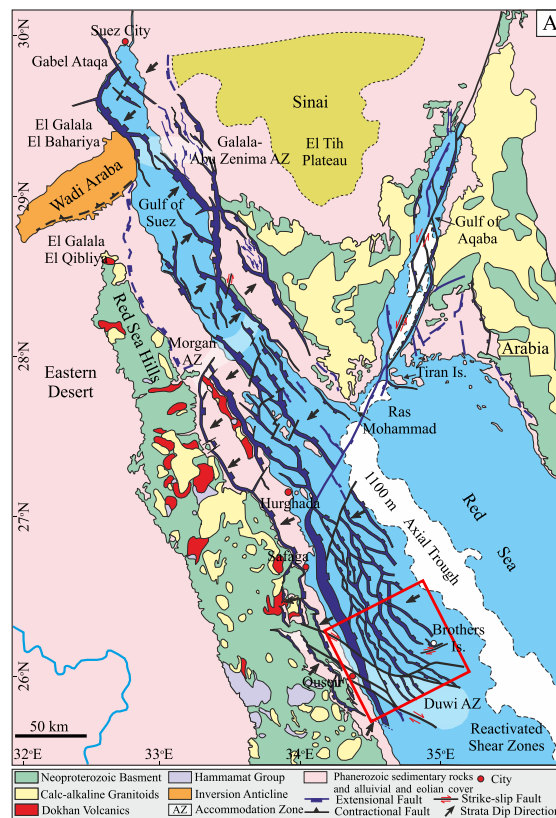
2. Geological Setting of the NRS

Most of the Red Sea geology information comes from onshore stratigraphic and structural data and offshore geophysical data. Only 14 exploratory wells have been drilled in the Egyptian Red Sea margin for hydrocarbon prospecting in the last 50 years, and little associated data are in the public domain. In addition, offshore seismic interpretation is severely limited by a thick layer of syn-rift evaporites (e.g., Cochran, 1983; Le Magoarou et al., 2021; Rowan, 2014). As a result, the structure and the nature of the crust that floors the NRS is still a matter of debate (e.g., Augustin et al., 2021).

Observations from onshore (Bosworth, 1994; Bosworth et al., 1998, 2020; Jarrige et al., 1990; Khalil & McClay, 2001, 2009; Moustafa & Khalil, 2020), and commercial well-drilling (Bosworth et al., 2020; Miller & Barakat, 1988; Tewfik & Ayyad, 1982) suggest that the tectonostratigraphic succession of the NRS margins can be roughly subdivided into the following:

1. Pre-rift sequence, formed by igneous and metamorphic basement and Late Cretaceous to Early Cenozoic sedimentary rocks;
2. Characteristic syn-rift sequence, composed of predominantly clastic strata followed by Middle to Late Miocene massive halite and layered evaporites;
3. Mainly siliciclastic syn-rift sequence formed by Pliocene-Pleistocene deposits (Figure 1b).

1   The crystalline basement of the Egyptian Red Sea rifted margin and the Eastern Desert formed during the Neoproterozoic and resulted from several magmatic and metamorphic phases developed during the Pan-African orogeny. Several studies on the basement composition and structures in the onshore outcrops have documented significant, complex Pre-Cambrian tectonic events (Johnson, 2014; Rogers et al., 1978; Stern et al., 1984). Conversely, only a few exploratory wells penetrated the Egyptian offshore basement, but the information has remained relatively poorly studied. Four boreholes north of Quseir (RSO-X 94-1; RSO-B 96-1; Figure 2a; Barakat & Miller, 1984; Bosworth et al., 1993; Tewfik & Ayyad, 1982) cut through granodiorite and granite, while the southern wells (Quseir A-1X; Quseir B-1X; Figure 2a; Bosworth et al., 2020; Ligi et al., 2018; Moustafa & Khalil, 2020) penetrated metamorphic rocks, including gabbros, suggesting a complex and still not entirely deciphered basement architecture. The results of the drilling program in the Egyptian Red Sea margin suggest that the Pan-African basement is present for several tens of kilometers offshore from the Western coastline. However, its composition and structure may be highly variable. Geochronological and geochemical analyses of gabbros drilled at the Quseir B-1X well and sampled from Brothers Islands revealed an oceanic-type basaltic melt composition and a cooling age of 25 ± 6 Ma (^{40}Ar/^{39}Ar), suggesting intrusion/underplating of mid-ocean ridge basalts melt as a consequence of a thermal event during the initial phase of the Red Sea rifting (Ligi et al., 2018). Therefore, the Brothers gabbro was interpreted as a lower crust intrusion of asthenospheric melt that predated the onset of rift and then was exhumed above the sea level due to a significant uplift of an extensional fault footwall (Bonatti et al., 2015; Bonatti & Seyler, 1987; Guennoc et al., 1988; Ligi et al., 2018; Taviani et al., 1986). South far of the Brothers Islands, Zabargad Island represents an uplifted block of lithosphere, this block includes three distinct upper mantle peridotite bodies. The existence of peridotites provides an example of "preoceanic," rather undepleted mantle bodies (Bonatti et al., 2015).

The pre-rift sedimentary sequence of the NRS rift is very similar to that of the southern Gulf of Suez (Figure 1b). Pre-rift strata involve three primary rock sequences (Nubia sandstones, mixed facies section, carbonate section; Khalil & McClay, 2017, 2020). These units are formed by shallow-water carbonate and siliciclastic rocks directly overlying the Precambrian basement and gradually thickening toward the northwest. The Upper Eocene and Lower Oligocene sedimentary records are missing in the Egyptian Red Sea, the southern Gulf of Suez (Moustafa & Khalil, 2020), and the Komombo basin in southern Egypt (Ali, Ali, et al., 2022; Ali et al., 2019).

A

Map labels: Suez City, Gabel Ataqa, El Galala El Bahariya, Wadi Araba, El Galala El Qibliya, Red Sea Hills, Eastern Desert, Gulf of Suez, Galala-Abu Zenima AZ, Sinai, El Tih Plateau, Gulf of Aqaba, Morgan AZ, Tiran Is., Arabia, Ras Mohammad, Hurghada, Red Sea, 1100 m Axial Trough, Brothers Is., Qusair, Duwi AZ, Reactivated Shear Zones, 50 km

Latitude marks: 30°N, 29°N, 28°N, 27°N, 26°N. Longitude marks: 32°E, 33°E, 34°E, 35°E

Legend: Neoproterozoic Basement; Calc-alkaline Granitoids; Dokhan Volcanics; Hammamat Group; Inversion Anticline; Phanerozoic sedimentary rocks and alluvial and eolian cover; City; Extensional Fault; Strike-slip Fault; Contractional Fault; Strata Dip Direction; AZ Accommodation Zone

B — Simplified stratigraphic chart

Age		Offshore NW Red Sea Rock Units	Lithology	Onshore NW Red Sea Rock Units	Lithology	Rift Phase	Seismic Sequence
Quaternary				Samadi / Shagara		Syn-rift	Pliocene Recent
Pliocene	Late / Early	Shukheir		Mersa Alam			
Miocene	Late	Zeit / South Gharib	Evaporites	Um Gheig / Abu Dabbab			Layered Evaporites & Halite
	Middle	Belayim / Kareem	Clastics	Syateen / Um Mahara			Syn-rift sediments
	Early	Up. Rudeis / L. Rudeis / Nukhul		Ranga			
Oligocene		Abu Zenima (Volcanics)		Nakheil-Abu Ghusun (Volcanics)		Pre-rift	
Eocene	Late	Darat					Pre-rift sediments
	Middle	Darat					
	Early	Thebes		Thebes			
Paleocene		Esna Shale		Esna Shale / Tarawan			
Cretaceous (Late)	Campanian / Maastrichtian	Sudr	Nubia A Nezzazat Group	Dakhla Shale / Duwi / Quseir			
	Santonian / Coniacian	Matulla					
	Turonian	Wata		Nubia			
	Cenomanian	Raha					
	Early (or older)	Malha					
Precambrian		Basement		Basement			Basement

Lithology legend: Sandstone; Shale/Claystone; Red beds & Cong.; Marl; Limestone; Shaly; Evaporites; Volcanics; Chert; Granite; Metasediments; Hiatus; Dolomite; Phosphate

Figure 1. (a) Simplified geological map of the northern Red Sea (NRS) region, modified from Ben-Avraham (1985), Bosworth et al. (2017), Bosworth and McClay (2001), Ehrhardt et al. (2005), Hughes et al. (2000), Khalil and McClay (2001, 2009). Red box indicates the study area. (b) Simplified stratigraphic chart of the onshore and offshore northern Red Sea, modified from Bosworth et al. (2020), Khalil and McClay (2017, 2020), and Moustafa and Khalil (2017).
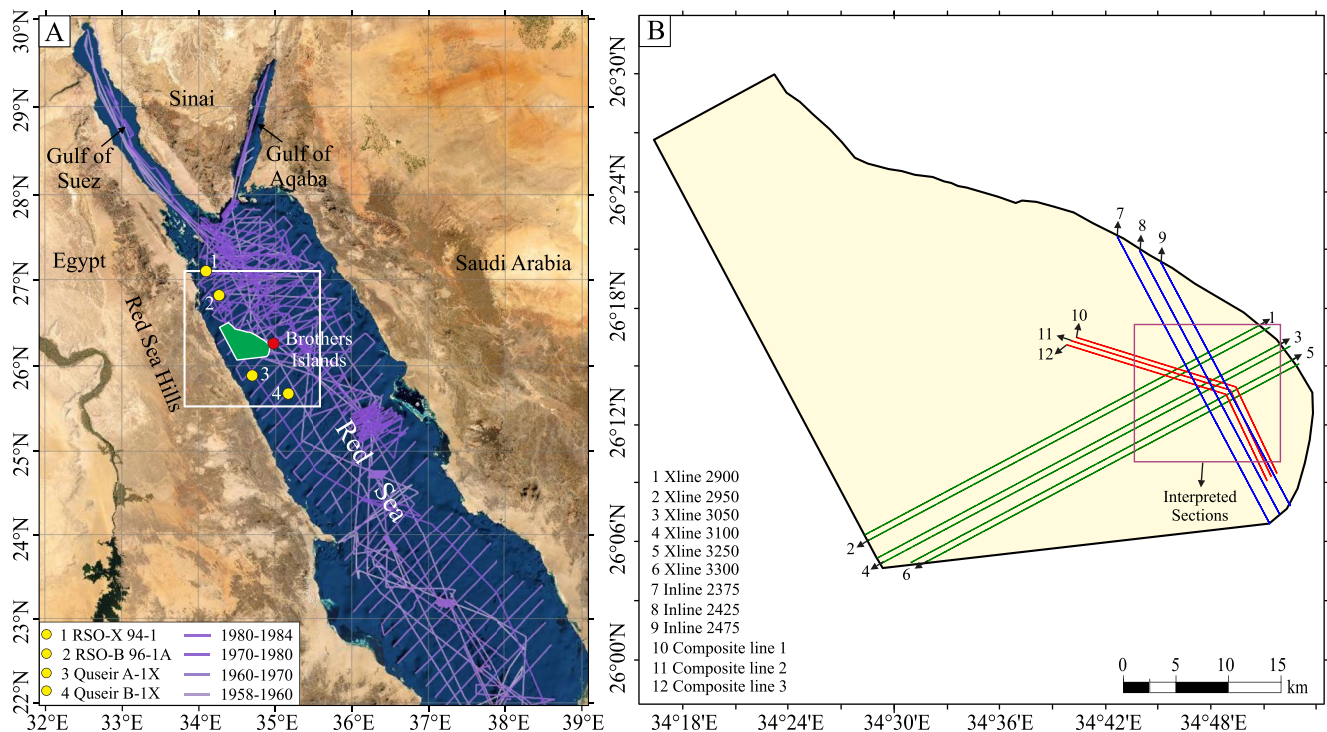
Figure 2. (a) Regional map showing the boundaries of the used geophysical databases: seismic, magnetic, and gravity. The white box and green polygon represent the "extended discussion area" and the 3D seismic survey, respectively. The purple lines indicate 12 ship tracks with both magnetic and gravity surveys between 1958 and 1986. (b) Detailed map showing the 2D seismic lines interpreted from the original British Gas 3D seismic reflection database.

2 The NRS and Gulf of Suez syn-rift units are usually divided into an early rift section and a main syn-rift section (Figure 1b). (a) The early rift sediments include the Nakheel Formation red beds and the Abu Zenima Formation in the NW Red Sea basin and the Gulf of Suez. They are overlain by 24–22 Ma volcanic rocks (Bosworth, 2015). (b) The main syn-rift sequence, during which tectonically driven subsidence was most rapid, is composed of a lower succession of siliciclastic rocks and an upper section formed by thick halite and layered evaporite sequences (Figure 1b). Carbonate units are volumetrically limited but represent regionally correlatable stratigraphic events. Several lines of evidence suggest that the entire Red Sea basin desiccated at the end of the Miocene age when it became subaerially exposed (Mitchell et al., 2017). This event resulted in widespread, major unconformity surface (post-Zeit), usually reported in the Red Sea literature as the "S-reflector" (Girdler & Whitmarsh, 1974; Mitchell et al., 2010; Ross & Schlee, 1973), which marks the base of post-evaporitic section.

3 During the Early Pliocene, most of the present-day NRS and the Gulf of Suez areas were flooded by open marine waters entering the Indian Ocean via Bab el Mandeb Strait (Said, 1990). Pliocene rocks include sandstone, claystone, limestone, and occasional gypsum, described with various formational names (Figure 1b). At the end of the Pliocene, an unconformity surface is observed in the Red Sea onshore. In contrast, the Pliocene-Recent sequence offshore is more complete and formed by sandstones, generally referred to as the Shukheir Formation (Bosworth et al., 2020).

The northwestern Red Sea and the Gulf of Suez display similar structural patterns characterized by zig-zagging faults that overall trend parallel to the rift strike (Jarrige et al., 1990; Montenat et al., 1988; Patton et al., 1994; Tewfik & Ayyad, 1982). Several km-scale tilted blocks bounded by major normal faults striking NW-SE have been described in the literature (Figure 1a; e.g., Khalil & McClay, 2001). At and south of Quseir, the Egyptian coast is dominated by a sizable onshore half-graben generated by a west-dipping master fault (the "Gebel Duwi fault") that runs sub-parallel to the shoreline (Figure 1a). Offshore, the system is complicated by several irregular salt domes and many prominent salt walls that lead to complex structural patterns, especially at depth (Bosworth et al., 2020; Gordon et al., 2010; Mitchell et al., 2019). Faults cut the syn-kinematic Rudeis, Kareem, and Belayim Formations, as evidenced by interpretations on the published seismic profiles, but the presence of salt challenges

the identification of deep structures on the seismic profiles. Therefore, the interpretation of the offshore fault system is mainly related to shallow structures at the interface with the seismic basement (Figure 1a). A limited number of published seismic sections show similarities in the structural setting of the near-shore margins of Saudi Arabia and Egypt, while the conjugate distal margins have a different structural style (Stockli & Bosworth, 2019). Detachment fault systems have been observed in the Midyan area of Saudi Arabia and along the Egyptian shoreline (Bosworth & Burke, 2005; Mougenot & Al-Shakhis, 1999; Stockli & Bosworth, 2019). Stockli and Bosworth (2019), interpreted a NE-SW 2D seismic section in the distal Egyptian margin and observed two NE dipping low-angle normal faults rooted in the continental crust.

The setting of the NRS was also influenced by the formation of the Dead Sea transform that accommodated a northeastward displacement of the Arabia plate relative to the Sinai sub-plate. Phases of left-lateral shear along this fault system that presently runs from the Red Sea rift in the Aqaba Gulf to the Maras Triple Junction in SE Turkey may have influenced the NRS structural architecture. The system has been active since Mid-Late Miocene up to the present, with a prominent post-Pliocene pulse (Bosworth & Burke, 2005; Girdler, 1990; Quennell, 1951, 1958). The Egyptian offshore fault system cuts entirely through the Late Miocene and Pliocene-Recent succession in the Hurghada offshore region. This is probably related to the young movement associated with the Dead Sea Transform activity in the NRS (Bosworth et al., 2020).

## 3. Data Sets and Methodology

Three different types of geophysical data were used to investigate and model the possible nature of a structural/morphological high that characterizes the study area (Figure 2). Gravity and magnetic public domain data sets covering a zone larger than the study area were used to integrate and extend interpretations of 3D seismic reflection data offshore Quseir. Geophysical data were processed at the Geophysics Laboratory of Khalifa University.

3.1. Seismic Data

3D seismic data were used to interpret the subsurface structural and seismo-stratigraphic elements of the study area. The database was acquired in 1999 by British Gas and covered 1,600 km^2 offshore central Egypt between Safaga and Quseir and west of the Brothers Islands (Figure 2; Gordon et al., 2010). Time migrated, reflection seismic profiles are organized in NW-SE oriented inlines and related orthogonal crosslines, 25 and 12.5 m spaced, respectively. Seismic reflection data allow the imaging of subsurface structures down to 7 s two-way time (TWT). The seismic interpretation process includes the recognition and picking of the principal seismo-stratigraphic features and faults (carried out using the Schlumberger Petrel^{TM} package) in order to define boundaries of the main seismo-stratigraphic units in the study area, and in particular, in the vicinity of the structural high (Ali, 2020; Ali et al., 2018; Ali, Abdelhady, et al., 2020; Ali, Abdelmaksoud, et al., 2020). Accordingly, six crosslines, three inlines, and three composite lines were interpreted to study the break out of the studied feature (Figures 2b, 3, 4, and 6). Several seismic attributes were applied and tested to resolve the surrounding evaporites and basement volume. We found that the root mean square amplitude (RMS) was the most effective (Figure 5). Time slices were generated from the seismic volume to delineate the shape of the studied landform (Figure 5). Two-way travel times were converted to depth, assuming an average interval velocity of 1.525 km/s for the seawater layer and 1.9 km/s for the Pliocene-Recent sediments (Table 1; Figure 7; Ligi et al., 2018; Mitchell et al., 2019). The obtained geological sections were used as an input for the 2D gravity/magnetic forward modeling and to delineate the 3D shape of the seamount.

3.2. Gravity Data

Free-air gravity data of the entire NRS were extracted from the 1-min satellite-derived global grid (version 31) of Sandwell et al. (2014) to analyze anomalies at the regional and local scale of about 175×175 km^2 (Figure 8). Gravity-field accuracy derived from satellite altimetry depends on altimeter range precision, spatial track density, and diverse track orientation. The current version of the altimeter-derived gravity field has an accuracy of about 1 and 2 mGal with improvements mainly in the 12–40 km wavelength band that is of interest for studying structures up to 6 km. Bouguer gravity data were obtained from the WGM2012 global gravity model (Bonvalot et al., 2012) provided by the Bureau Gravimétrique International; WGM2012 Bouguer gravity anomalies derive from the Earth global gravity models EGM2008 and DTU10 corrected (using a reference density of 2,670 kg/m^3) for
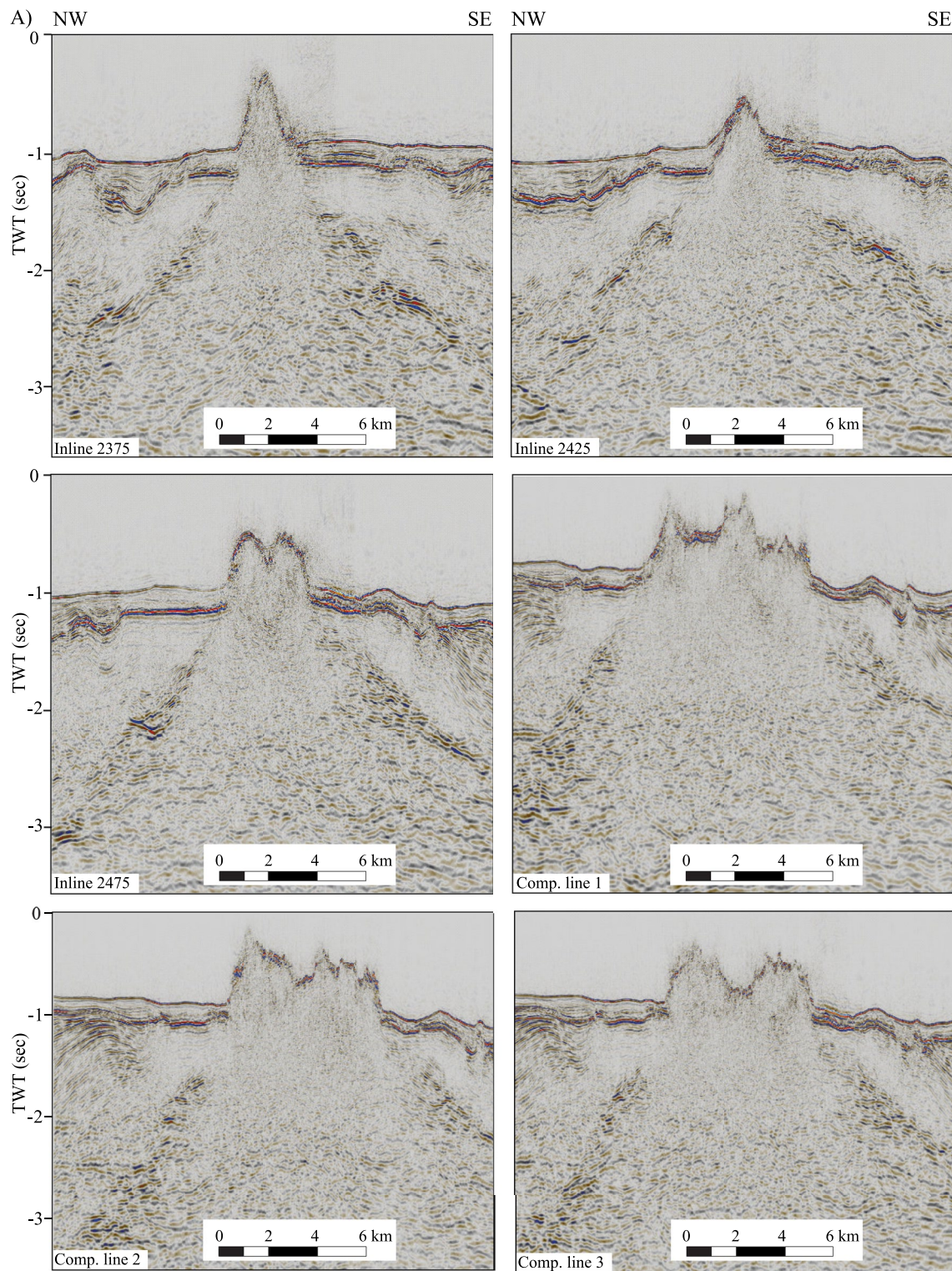
Figure 3. (a) Uninterpreted and (b) interpreted seismic sections (locations in Figure 2b) showing the different architecture of the basement structural high. White lines represent extensional faults, the yellow arrow prominent sills, and the dashed line a major difference in basement amplitudes (see also Figure 5).
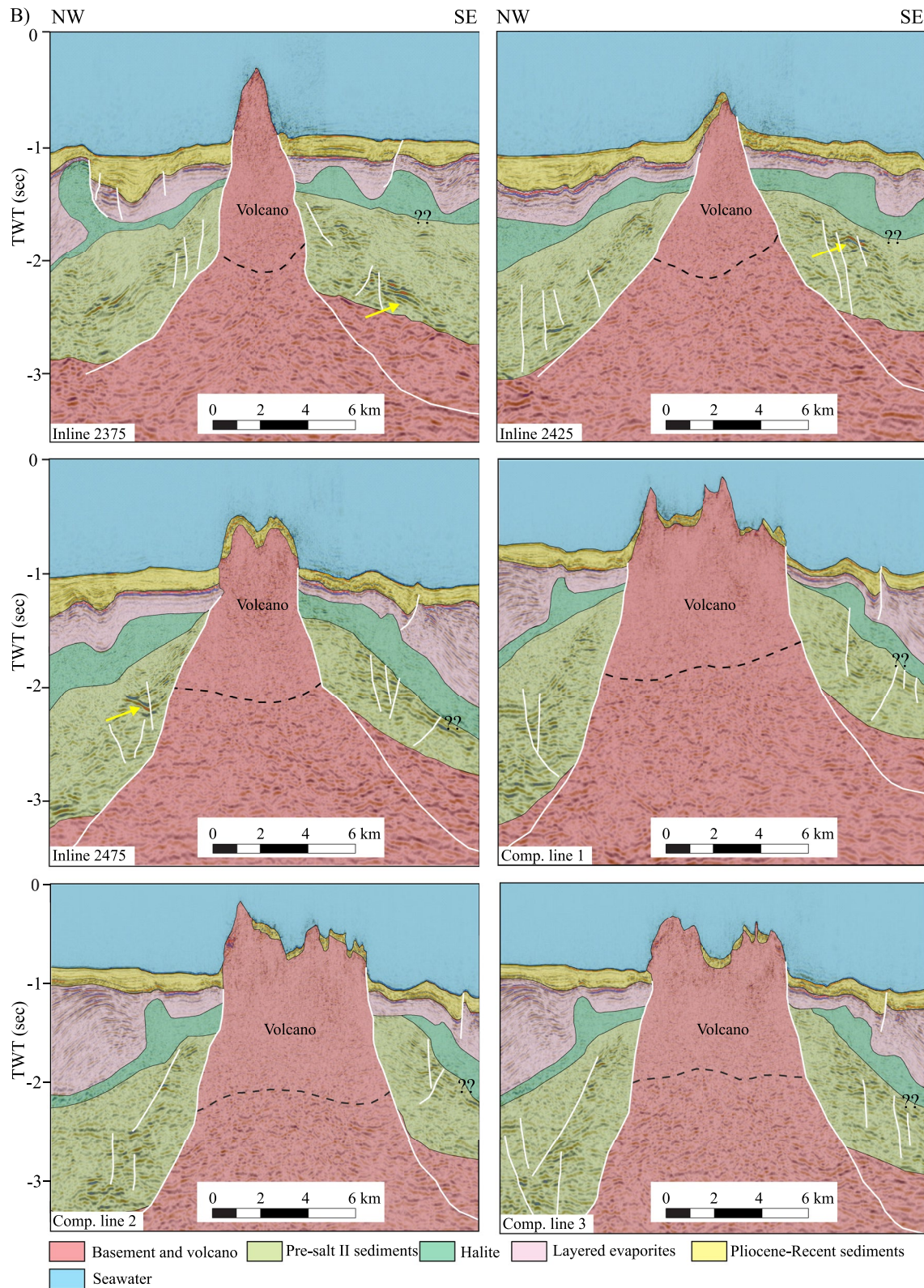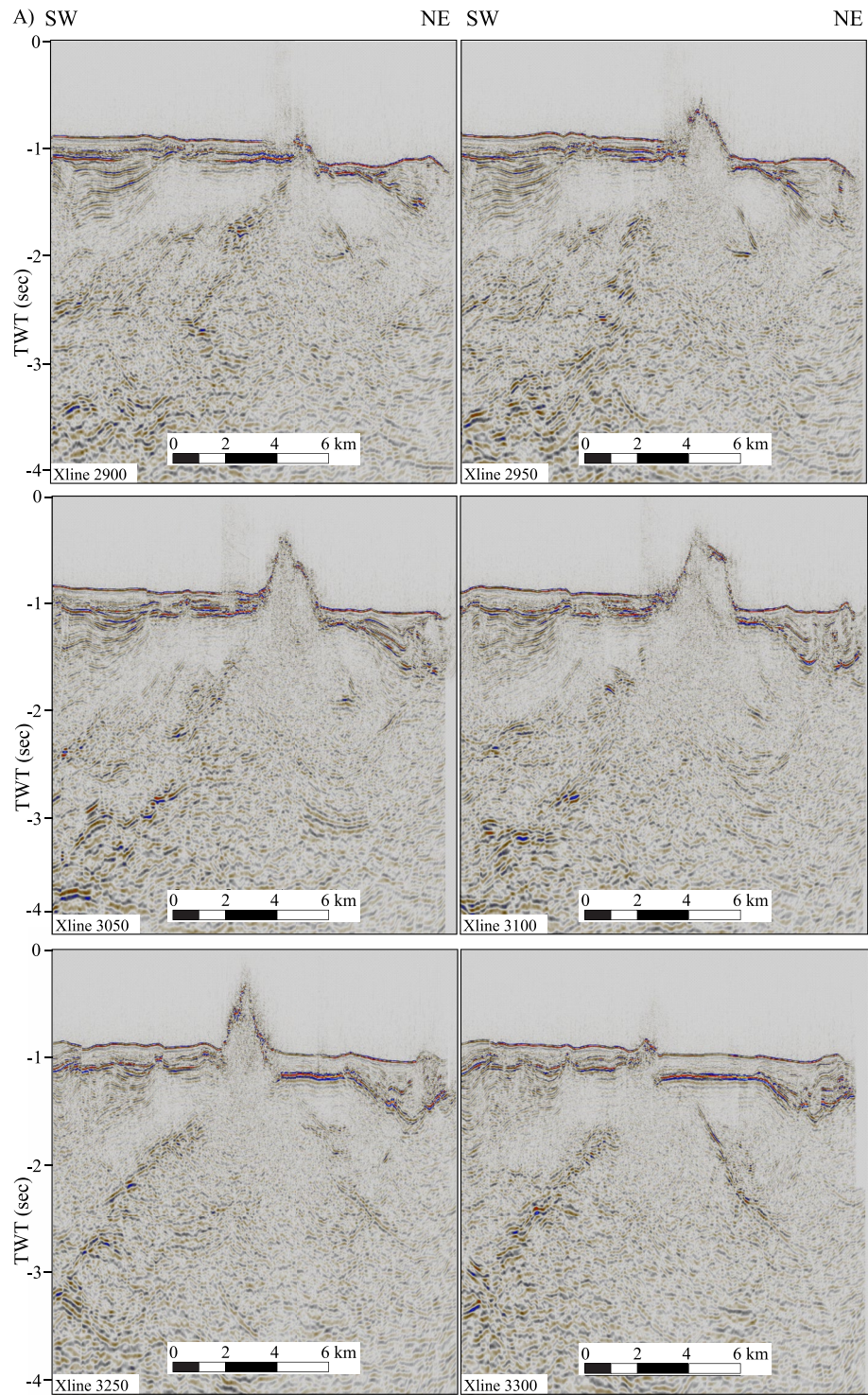
Figure 3. (Continued)

Figure 4. (a) Uninterpreted and (b) interpreted seismic sections (locations in Figure 2b) showing the different architecture of the basement structural high. White lines represent normal faults, the yellow arrows indicate sills and the dashed black line is the base of the seamount.
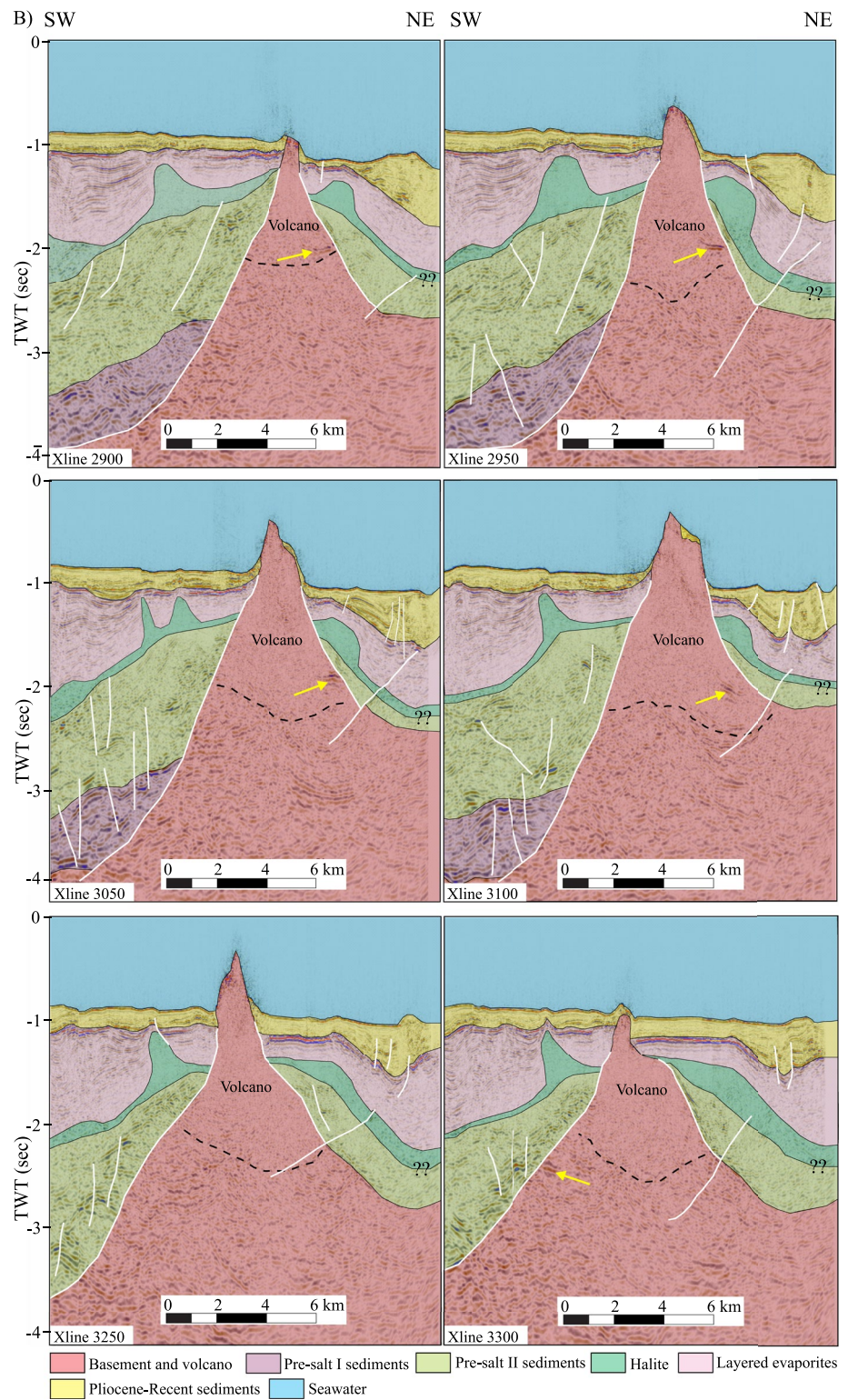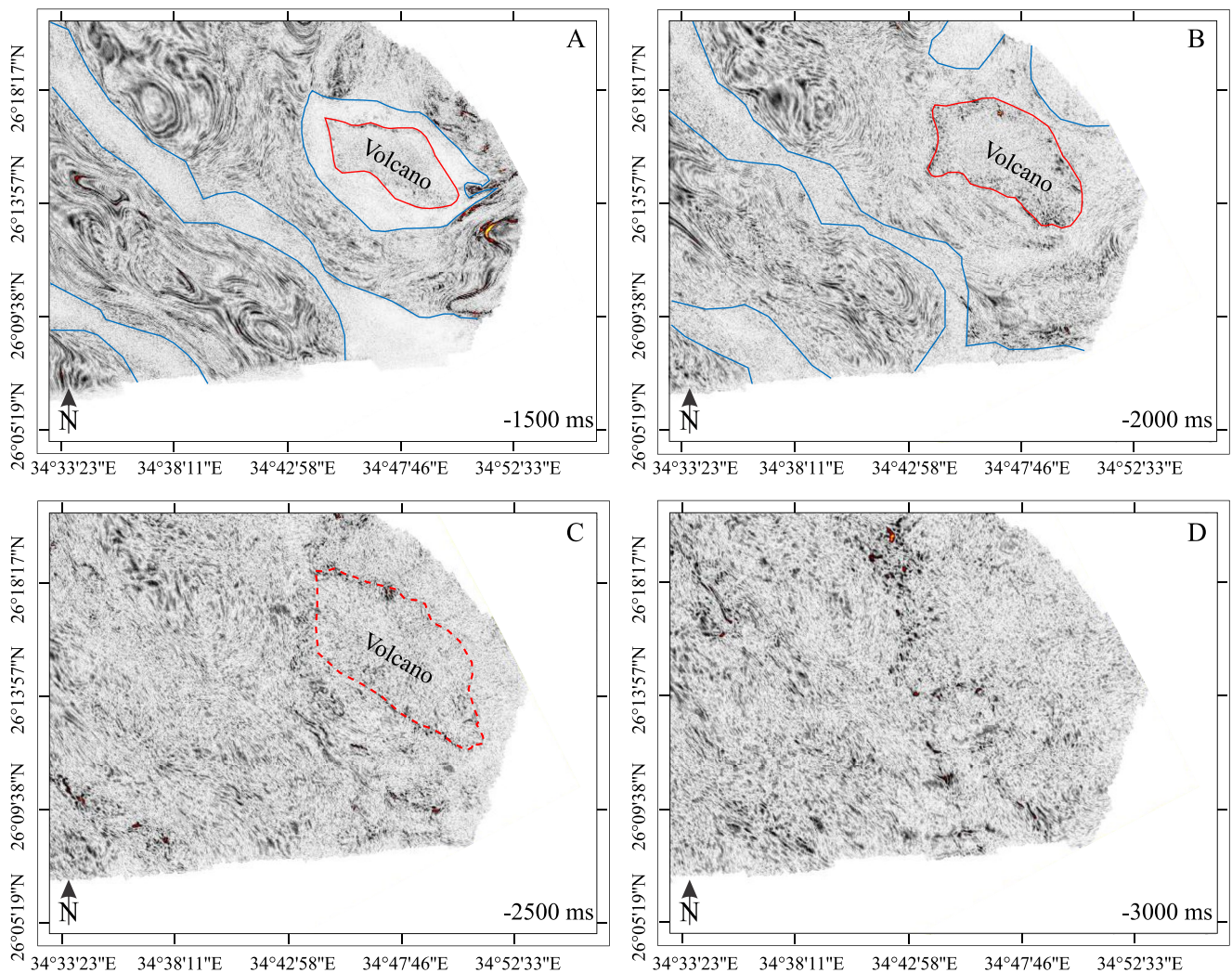
Figure 4. (Continued)

Figure 5. Time slices of the studied structural high. Areas of distinctly different reflectivity texture are delimited by red and blue lines. Seismic amplitudes allow to delineate areas (and volumes) with different acoustic responses. Note the progressive enlargement with depth of the area having anomalous RMS reflection amplitudes (red contour) surrounded by halite (blue contour; A and B). In (c) the anomaly is localized inside the seismic basement, while in (d), the anomaly disappears. These features are interpreted as horizontal sections at increasing depth within a volcanic edifice. See Figure 2b for location.

surfaces masses contributions based on the 1 arc-minute global relief model ETOPO1 (Balmino et al., 2012). Five high-pass filters were applied to the Bouguer data to generate distinct maps from the study area with wavelengths lower than 5, 10, 25, 50, and 100 km (Figure 9). A NE-SW Bouguer gravity profile along crossline 3,200 of the 3D seismic block was extrapolated to perform the forward model (see Subsection 3.4).

3.3. Magnetic Data

A magnetic anomaly map of 2 arc-minutes (about 3.7 km) resolution was generated from the Earth Magnetic Anomaly Grid (EMAG2$_{v3}$). EMAG2$_{v3}$ consists of a global grid compiled from satellite, ship, and airborne magnetic measurements (Meyer et al., 2017). Magnetic anomaly values are evaluated at the reference elevation of 4 km, and each grid value comes with an error estimate (Meyer et al., 2017). Regional and local maps were extrapolated to discuss the magnetic features at different scales (Figure 10). The magnetic anomalies were reduced to the pole (RTP; Cooper & Cowan, 2005; Keating & Zerbo, 1996; Li, 2008) to remove the effect of induced magnetization and strike on the shape of magnetic anomalies (Figure 10c). A high-pass filter was applied on the RTP grid with different wavelength cutoffs (10, 25, 50, and 100 km; Figure 11) to focus on the high-frequency content of the signal and enhance the resolution of the magnetic anomalies in the study area. A
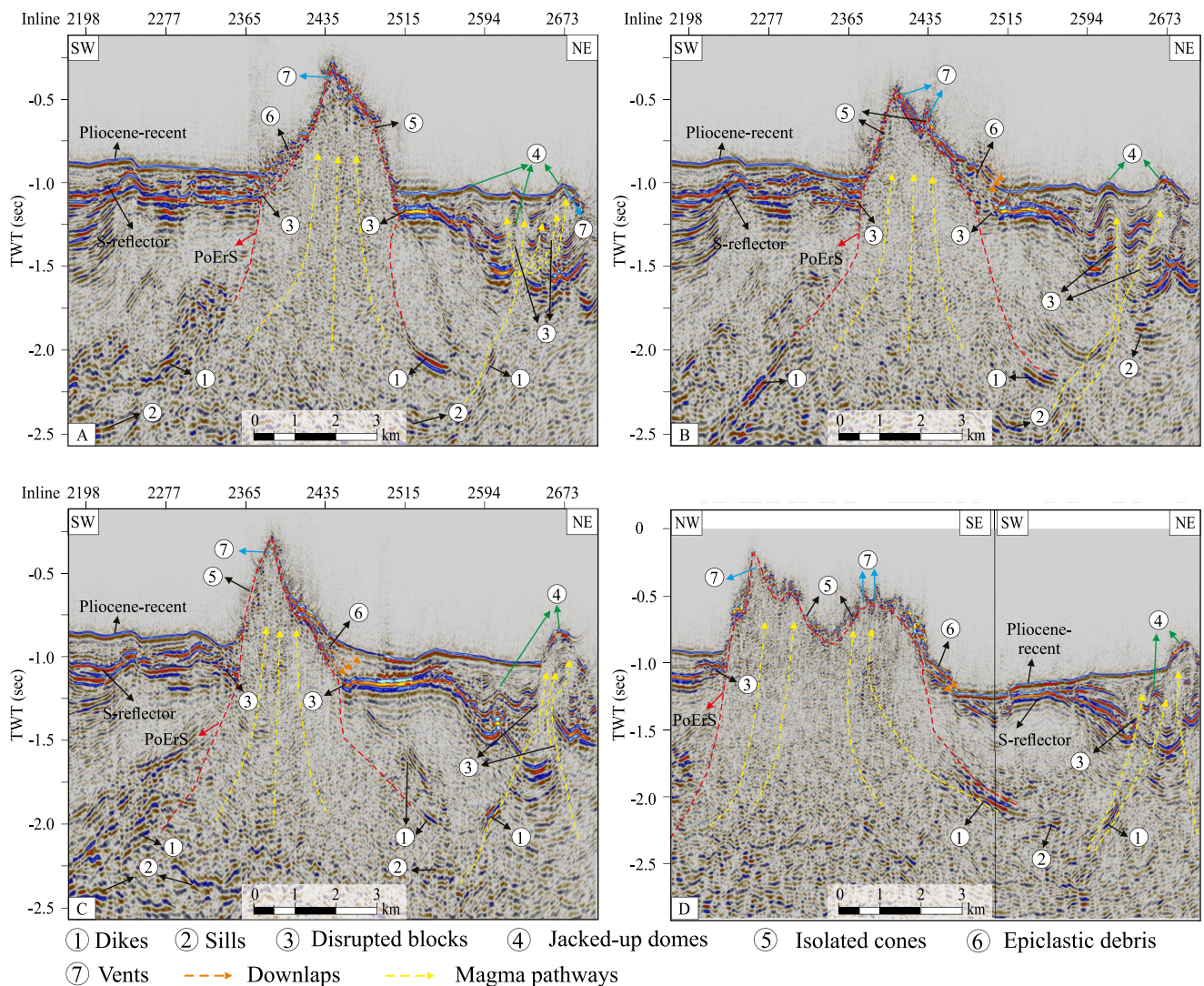
Figure 6. Interpretation of relevant seismic features related to the morphology of the volcanic edifice. The interpreted seismic sections show six architectural elements which are associated with a volcanic edifice.

NE-SW RTP magnetic profile corresponding to the position of crossline 3,200 of the 3D seismic survey was extrapolated to build a 2D forward model (see Subsection 3.4).

3.4. Forward Modeling

A two-dimensional forward model of magnetic and gravity anomalies was generated to test the geophysical response of the interpreted geology based on 3D seismic data and stratigraphic information from the published exploration wells drilled in the area between 1970 and 2010. The 46 km-long crossline 3,200 extracted from the 3D seismic survey was used to set up the geological model. The GM-SYS profile tool of the Oasis Montaj® software was used for the forward modeling. Different seismic horizons derived from the interpretation of the crossline 3,200 have been included in the model. In detail, they mark the top of the following units: the basement high (seamount), the Pliocene-Recent sediments, the layered evaporites, the massive halite, the pre-salt sediments, and the pre-rift seismic basement (Figure 12). The horizons were depth converted using an average velocity for each stratigraphic unit (plus the water layer) as in Table 1. Densities and magnetic susceptibilities of the seismic layers are average values taken from the literature (Table 1). Parameters (densities and magnetic susceptibilities varying within the ranges indicated in Table 1) were adjusted to approach the best fit between the

Table 1
The Used Average Densities, Magnetic Susceptibilities, and Velocity of the Available Units in the Northern Red Sea (Almalki et al., 2014; Bonatti & Seyler, 1987; Cochran et al., 1991; Gettings et al., 1986; Makris & Rihm, 1991; Saleh et al., 2006; Salem et al., 2013; Shi et al., 2018)

Unit name	Average density (g/cm³)	Average susceptibility (μcgs)	Average velocity (m/s)
Seamount	2.65	3,400	3,500
Pliocene-recent sediments	2.3–2.35	0	1,900
Layered evaporites	2.40	0	3,000
Halite	2.2–2.25	0	4,200
Syn-rift sediments	2.4–2.55	0–25	2,700
Pre-rift sediments	2.53–2.55	0–50	2,800
Upper crust	2.7–2.8	450–1,000	3,500
Lower crust	2.72–2.82	1,200–6,000	–
Mantle	3.05–3.2	0	–

calculated magnetic and gravity values until observed magnetic and gravity anomalies were successfully achieved.

4. Results

Results from seismic interpretation, free-air and Bouguer gravity anomalies, and magnetic anomalies are discussed in detail in the following sections. Forward modeling results are reported in the Discussion.

4.1. Analysis of Seismic Data

Seismic data interpretation was focused on the region southwest of the Brothers Islands (Figure 2). The area corresponds to a seismic basement rise between two prominent rift-related normal faults (Figures 3, 4, and 6). Picking of the seismic basement, pre-salt, massive halite, layered evaporites, and Pliocene-Recent sequences was carried out and displayed using the same seismo-stratigraphic criteria as Ligi et al. (2018, 2019). Additional observations based on the reflection properties such as reflectivity, amplitude, frequency, and phase helped differentiate the deepest part of the pre-rift basement from that of the structural high to the SW of the Brothers Islands.

Four time slices of the RMS amplitude seismic attribute were selected from the 3D seismic volume to determine the location and extent of the basement of the structural high with varying depths in the time domain (Figure 5). The eastern half of the 3 s time-slice shows no significant changes in reflection amplitudes throughout the area, probably suggesting the presence of the crystalline basement only (Figure 5d). However, slight changes in the reflection amplitudes are observed in the northeastern area in the 2.5 s time-slice (red dashed polygon: Figure 5c), probably due to a change in the seismic properties of the basement, thus suggesting a different composition. The area with anomalous amplitudes has an average size of about 17 by 7 km at this depth (Figure 5c). Figures 3 and 4 show that the ridge elevation above the seafloor varies from the southeast to the northwest. The crossline 2,900 shows that the seamount is active through the entire Pliocene-Recent sequence, stopping its growth at the seafloor at about 0.9 s (TWT). The elevation above the surrounding seafloor significantly increases north-westward and reaches its maximum at about 0.33 s along crossline 3,250. Crossline 3,300 shows a drastic decrease in the height of the structural high down to 1 s, where it cuts the lower part of the Pliocene-Recent sequence without reaching the seafloor (Figure 4). Several sills and other intrusions within the sedimentary sequence have been recognized in crosslines 3,050 and 3,100 (Figure 4). At 2 s (TWT) depth, the structural high becomes sharper and forms a ridge, with borders easily distinguishable, in terms of RMS amplitudes, from the surrounding terrain. The shape of the ridge is oval in plan-view, elongated NW-SE, with a variable length from 17 to 13 km and width from 7 to 6 km at the depths of 2.5 and 2 s (TWT), respectively (Figures 5b and 5c). Two NW-SE elongate salt walls develop southwest of the ridge (Figure 5b). The 1.5 s time slice shows that the ridge is surrounded by halite (Figure 5a). The interpreted salt walls at 2 s continue in the 1.5 s time slice, where they become straighter and increase their width slightly.

Figure 7h displays the top of the seismic basement emerging from the surrounding seafloor. The part of the ridge that emerges from recent-most sediments is characterized by a peculiar shape, composed of two distinct sub-circular cones (Figure 7h). This feature is evident from the cross- and inline analyses (Figures 3 and 4). The southwestern sector of the seamount is thinner than the northeastern one and forms a very sharp peak that disappears toward the northeast beneath the Pliocene-Recent deposits (composite lines 1 and 2 in Figure 3). Three composite lines image the top surface of the ridge, which is irregular. Some reflectors interpreted as recent sediments can be observed overlying the volcanic edifice, between seamount culminations and flanks. These sediments are interpreted as post-depositional growth of the volcano (Figure 3).

Several detailed observations from the 3D seismic survey strengthen this interpretation. Following Bischoff et al. (2019), two principal surfaces can be recognized in a volcanic edifice: the pre-eruptive (PrErS) and post-eruptive (PoErS). These surfaces allow distinguishing pre-, syn- and post-magmatic sequences, which repre-
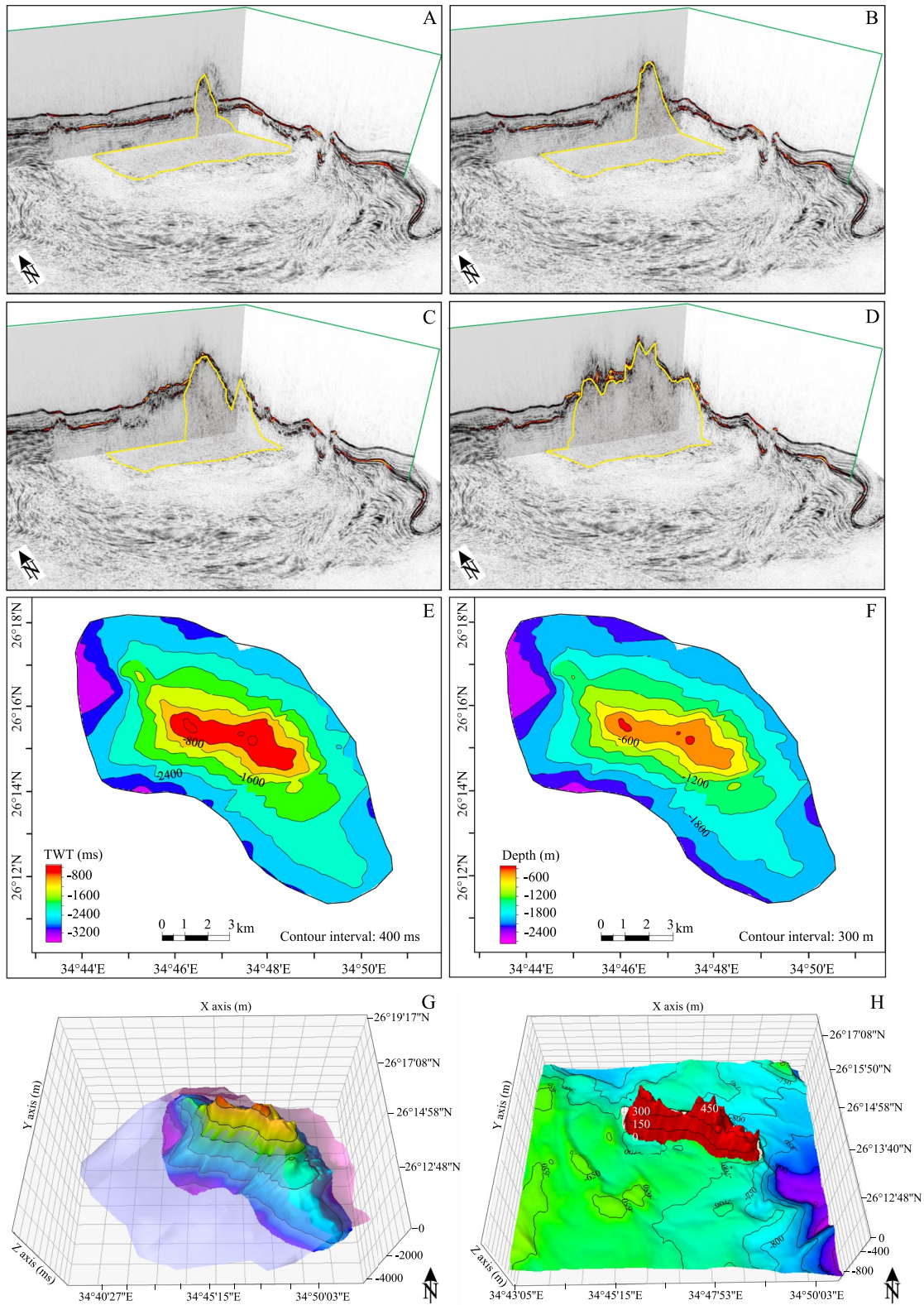
Figure 7. (a–d) 3D views of time slice at −1,500 ms with 4 composite lines in the NW-SE and NNW-SSE directions show 3D geometry of the seamount marked by a yellow polygon. (e) Two-way travel time (TWT) map of the top seamount. (d) Depth map of the top seamount. A 3D view of the top seamount in time (g) and depth (h) domain.
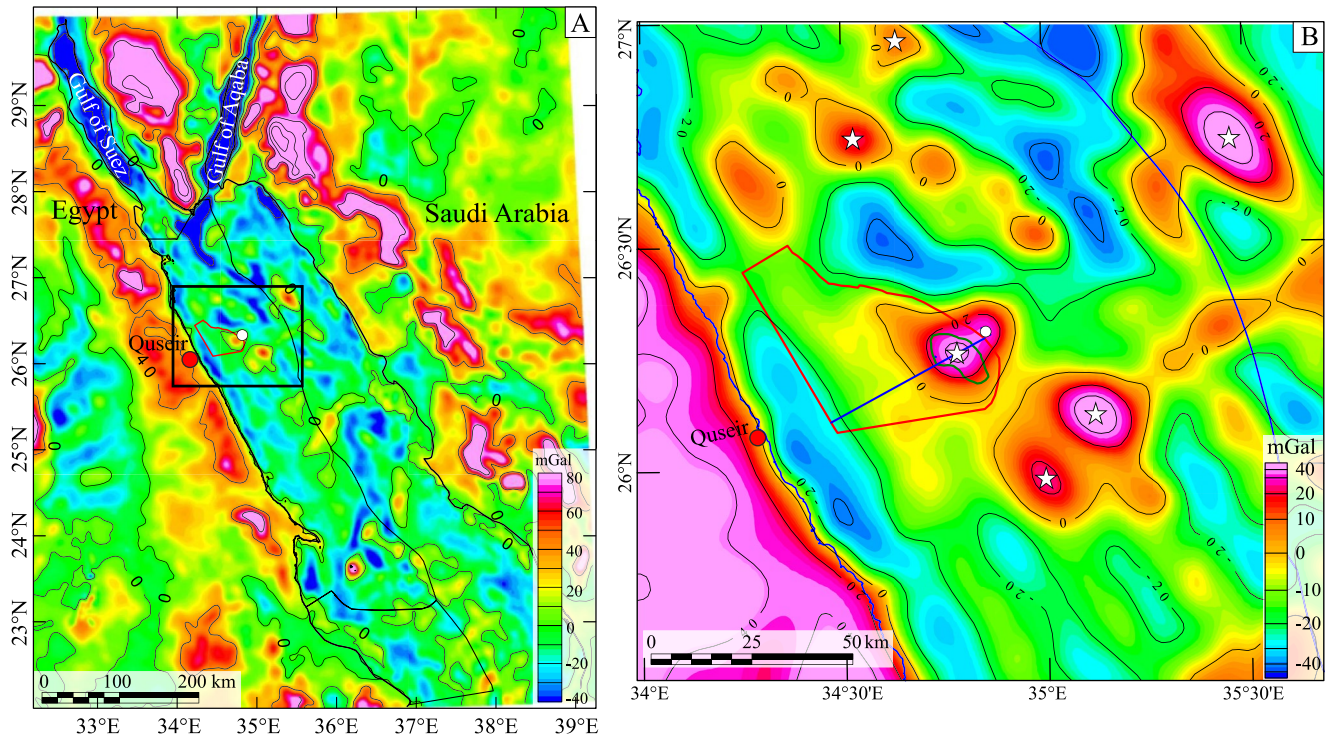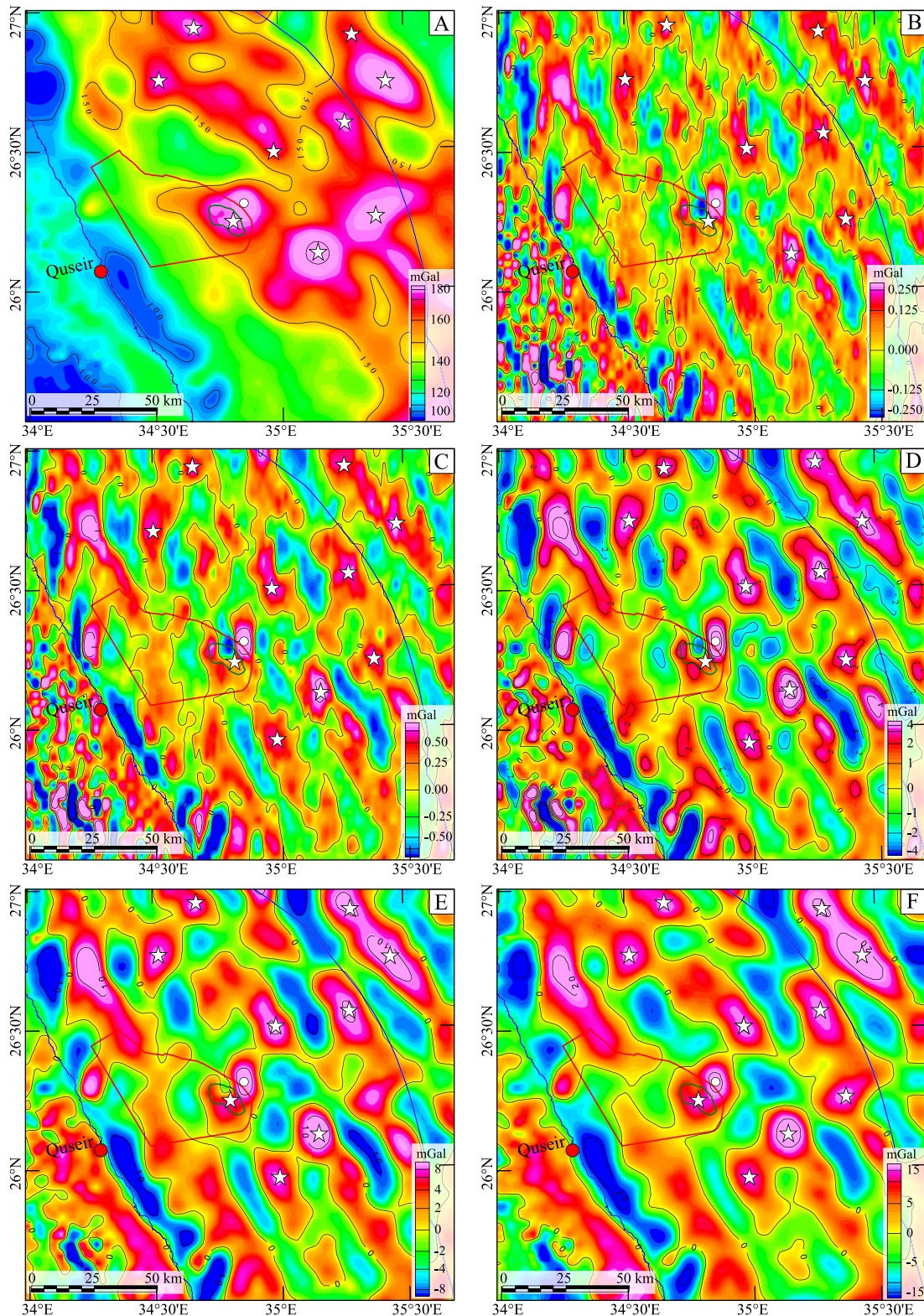
Figure 8. (a) Free-air gravity anomaly map of the northern Red Sea region. (b) Detail of the study area showing local significant gravity anomalies. The white dot indicates the position of the Brothers Islands; the white stars, suggested volcanic structures. The blue line represents the track of crossline 3,200 used to compute the gravity anomaly profile in Figure 12.

sent morphological elements easy to identify in a seismic section. Six classes of architectural elements have been interpreted in the study area (Figure 6).

1. *Dikes or minor magmatic bodies* characterized by sub-vertical or high-angle reflectors with high amplitude, located below the PoErS and within syn-rift sediments (Figure 6).

2. *Sills or sub-horizontal igneous bodies* showing low-angle, high-amplitude reflectors. They are common in the syn-intrusive sequence between 2.2 and 2.5 s, and are characterized by a lateral size up to 1 km and high amplitude reflectors. Figures 6a–6c display a complex network of dikes and sills that deform the pre-magmatic sedimentary layers. These intrusions probably derived from magma chambers.

3. Homogeneous sectors characterized by parallel, sub-horizontal reflectors that have been folded during magmatic activity and that display abrupt discontinuities that can be recognized in several seismic sections and have been interpreted as disrupted blocks (Figure 6). These disrupted blocks are usually located beneath the eruptive centers, as discussed by Bischoff et al. (2019). Their presence confirms the migration of melts through the sedimentary succession producing deformations such as folds, normal, and reverse faults at hundreds-to-thousands meter scale plan (e.g., Holford et al., 2012; McLean et al., 2017; Muirhead et al., 2016; Planke et al., 2005; Senger et al., 2017). A significant number of normal faults, folds, and jacked-up strata, probably related to such a process, have been recognized and shown in Figure 6.

4. *Jacked-up domes* derived by the uplift and doming of the PrErS sequence reflectors usually associated with high amplitudes (Bischoff et al., 2019). The sub-circular mounds observed in 3D views, with variable diameters from 0.5 to 2 km, are associated with the interpreted underlying magmatic activity (Figure 6).

5. *Cone-shaped morphology* of the seamount recalls that of a composite cone-type volcano (Jones et al., 2017; Lorenz & Kurszlaukis, 2007; Mitchell, 2001; White & Ross, 2011), characterized by a sequence of reflectors that accumulated around the vent zones and forms convex curvature. In the study area, the main volcanic body displays a single or multiple summit morphology, associated with a number of small cones, with a diameter ranging from 1 to 2 km. A small, isolated cone can also be recognized in the northeastern termination of the section (Figure 6c)

Figure 9. (a) Bouguer gravity anomaly map of the study area. Bouguer anomalies filtered with wavelengths (b) less than 5 km, (c) less than 10 km, (d) less than 25 km, (e) less than 50 km, and (f) less than 100 km showing good matching between the location of the volcano from the 3D seismic survey and the positive gravity anomaly from the filtered gravity data, as well the presence of several positive anomalies surround the Brothers Islands. White dot, Brothers islands; the white stars, suggested volcanic structures. The red and green polygons represent the 3D seismic survey and the location of the new volcano, respectively.
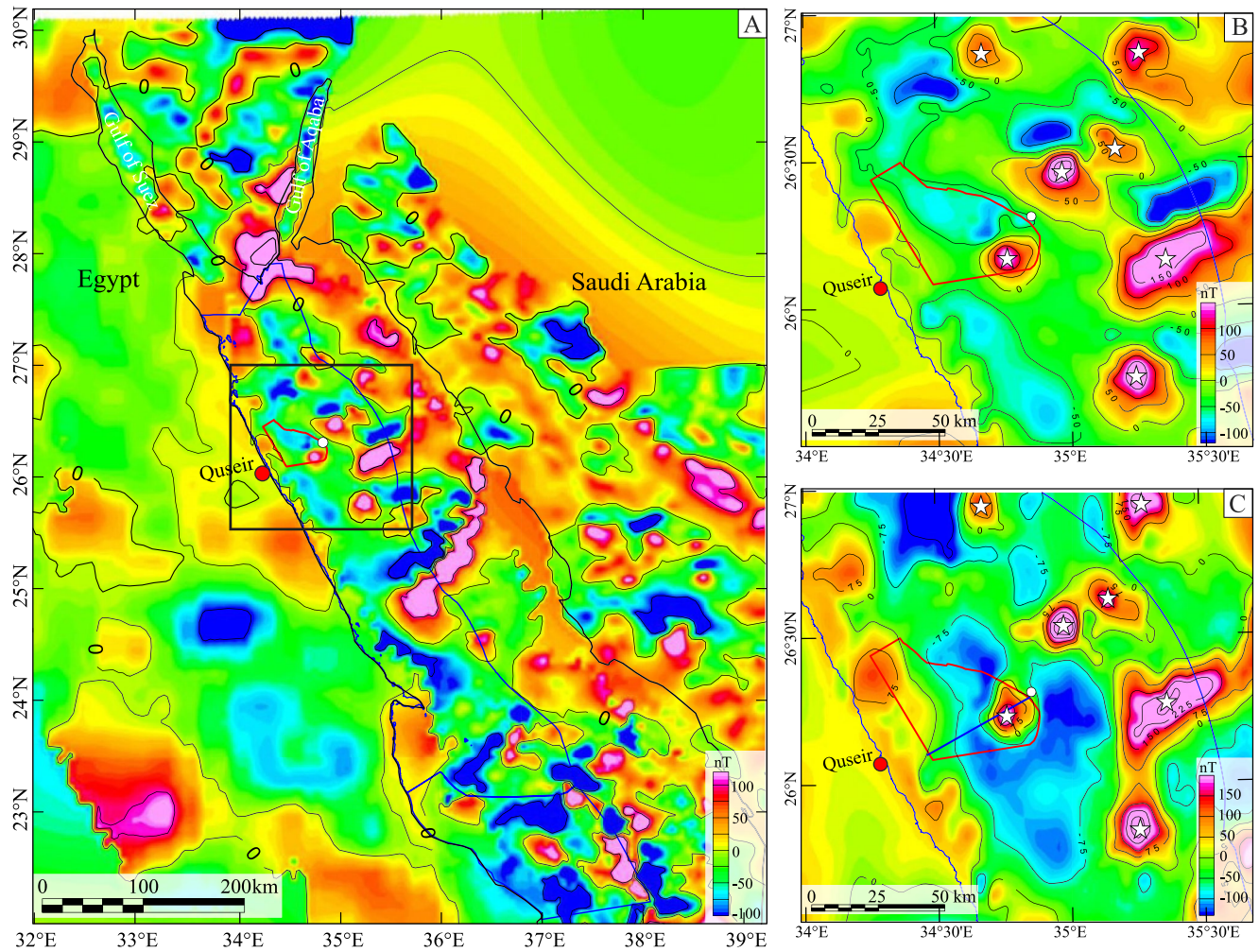
Figure 10. (a) Magnetic anomalies of the northern Red Sea. (b) Detail of the study area before and (c) after application of the reduced to the pole operator. The white dot indicates the position of the Brothers Islands; the white stars, the location of suggested volcanic structures and the blue line indicates the location of crossline 3,200 used to perform magnetic forward modeling of Figure 12.

6. A post magmatic apron of layered reflectors can be recognized on the flanks of the seamount (Figure 6a). This is particularly evident and developed along the northeastern flank, where seismic reflectors locally have a convex shape (Figure 6c) and down-lap on their substratum. This feature has been interpreted as a localized *epiclastic debris* accumulation ("epiclastic plume"), probably related to the erosion of the volcanic edifice.

Several 3D views were generated to illustrate the shape and physiographic features of the seamount, combining the 1.5 s time slice with four arbitrary lines in the NW-SE and NNW-SSE directions (Figures 7a–7d). Figures 7a and 7b image the northeastern sector of the seamount, which consists of one prominent cone with steep flanks. Laterally, it grads to a more complex morphology consisting of two or three main culminations above the surrounding seafloor forming small and steep cones (Figures 7c and 7d). The TWT contour map of the seamount surface (Figure 7e) has been used to produce a 3D view of the entire seamount (Figure 7g). Two-way travel times range from 0.28 to 3.2 s (Figures 7e and 7g). The TWT map has then been converted to depth using an average seismic velocity, given the complexity of the seismic unit geometries that probably lead to significant lateral and vertical velocity variations. The picked horizon was then gridded in depth-domain throughout the survey area to produce the structural map shown in Figure 7f (Ali et al., 2017a, 2017b). The depth of the submarine portion of the volcanic edifice (i.e., the seamount itself) ranges from 215 m bsl at its summit to approximately 735 m bsl at the contact with the surrounding seafloor, while the roots of the volcanic apparatus, buried under sediments and halite, reaches the depth of about 2,800 m bsl (Figures 7f and 7h). The 3D view shows that the seamount rises above the surrounding seafloor on average between 300 and 520 m (Figure 7h). The seamount is elongated
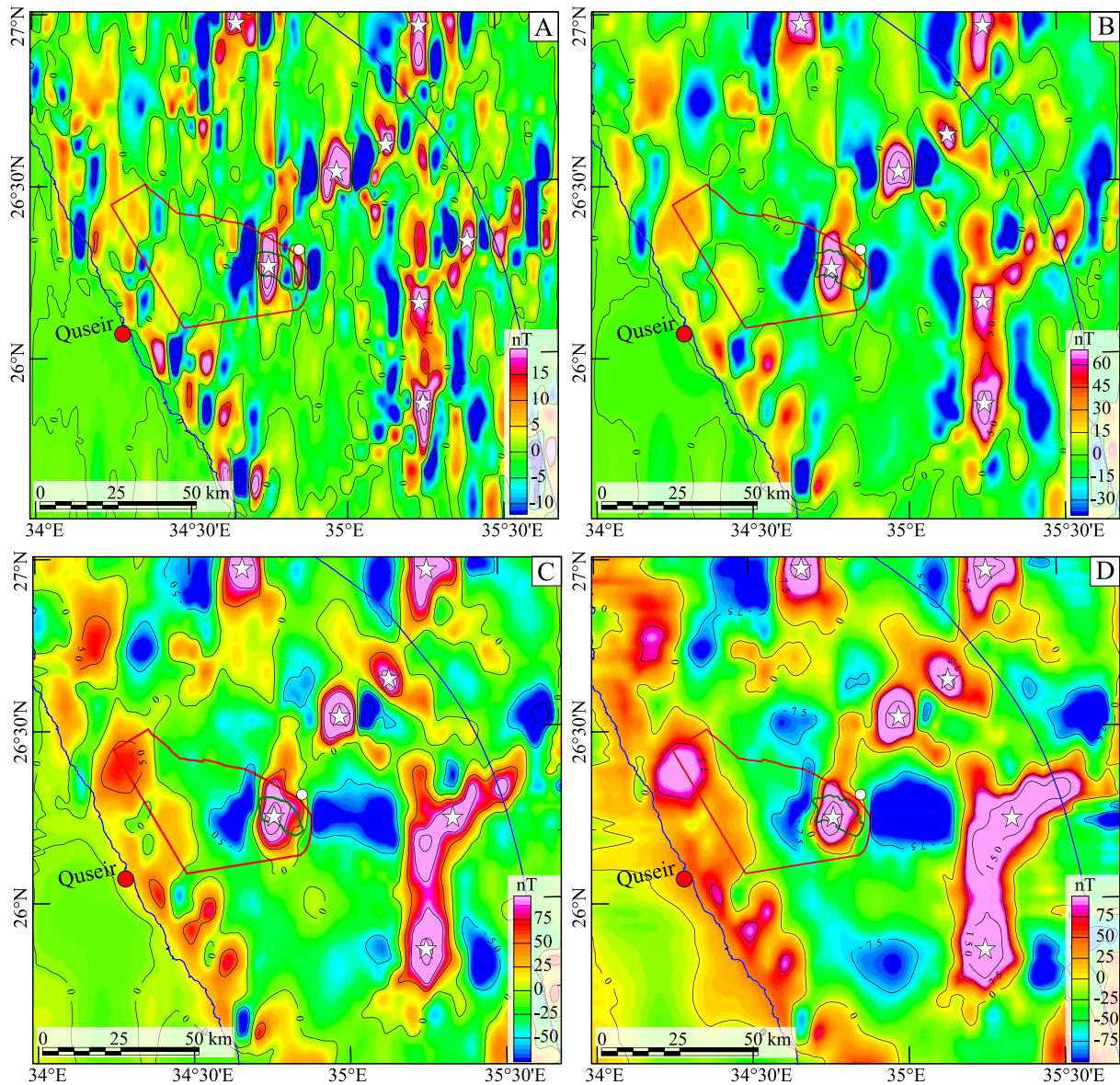
Figure 11. Filtered magnetic anomalies with wavelengths (a) less than 10 km, (b) less than 25 km, (c) less than 50 km, and (d) less than 100 km showing good matching between the location of the volcano from the 3D seismic survey and the positive magnetic anomaly from the filtered magnetic data. Some new volcanoes are also observed surrounding the Brothers Islands. White dot, Brothers islands (gabbro highs); the white stars, suggested volcanic structures. The red and green polygons represent the 3D seismic survey and the interpreted volcanic features, respectively.

toward the NW-SE direction, and the exposed sector measures 6 × 1.6 km, while the buried apparatus measures approximately 7 × 17 km (Figures 7e–7h). The seamount is dissected by two major normal faults running NW-SE for 15 km parallel to the seamount elongation axis. Figures 7a and 7b display the northeastern sector of the seamount consisting of a single major cone with steep flanks and dip-angles from 50° to 65°. The north-western and south-eastern ends have gentle flanks with a dip angle varying from 15° to 30°. In the middle part of the seamount, two major conical summits rise from the surrounding seafloor (Figures 7c and 7d).

4.2. Analysis of Gravity Anomalies

The regional free-air gravity anomaly map for the entire NRS rift system is shown in Figure 8. The free-air gravity anomaly values range from −40 to 80 mGal. A sharp transition between the positive and negative free-air gravity values is observed along the Egyptian and Saudi coastal lines and the Sinai Peninsula. This contrast is
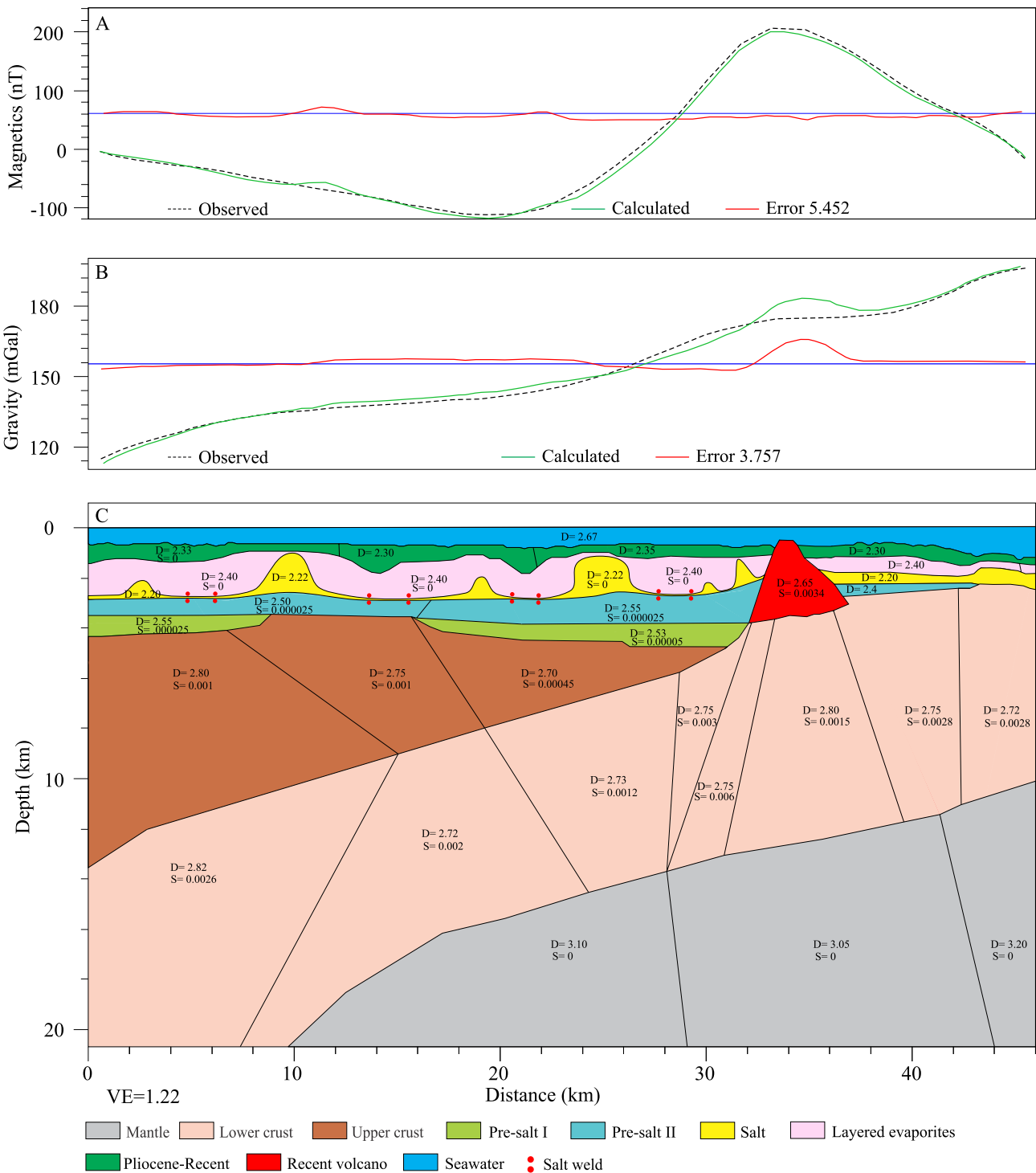
Figure 12. 2D forward model along crossline 3,200. (a) Observed versus predicted magnetic anomalies and (b) measured versus predicted Bouguer gravity anomalies. (c) A simplified cross-section was used to generate the best-fit model, where a volcanic edifice overlies the basement high. D and S indicate assumed density in g/cm^3 and magnetic susceptibility in cgs, respectively.

due to onshore, parallel to the coast, rough topographic belts (Hijaz and Asir Mountains on the Saudi side and the Red Sea Hills on the Egyptian side), which generate positive anomalies, while the negative anomalies along both shorelines are probably due to elongated, subsistent basins. The regional free-air gravity map shows that most of the NRS offshore margin is characterized by low free-air gravity values <10 mGal, except for a few

positive anomalies in the north (north of Quseir city). All of these positive gravity anomalies were interpreted by Cochran (2005), Cochran and Karner (2007), and Duncan and Al-Amri (2013) as volcanic seamounts.

A free-air gravity anomaly map for the study area was extracted to interpret the origin of the gravity anomalies in the surroundings of the Brothers Islands (Figure 8b). The study area shows free-air gravity values of −40–40 mGal. Several minor positive anomalies are observed in the northern and northeastern parts of the study area, and three significant positive anomalies with values of more than 20 mGal can be identified. Most of them have a continuous elongated shape trending NW-SE parallel to the rift axis and likely represent volcanic seamounts. Furthermore, the Bouguer anomaly map shows several positive anomalies with high values varying between 160 and 200 mGal (Figure 9a). Accordingly, a high-pass filter with different wavelength cutoffs (5, 10, 25, 50, and 100 km) was applied to the Bouguer anomaly grid to enhance the high-frequency content of the signals (Figures 9b–9f), however the high-pass filtered maps at 50 and 100 km show the best results with several isolated high positive anomalies (Figures 9e and 9f). These anomalies are aligned in the NE-SW direction and are almost elongated in the NW-SE parallel to the rift orientation (Figures 9e and 9f). One of these areas, located southwest of the Brothers Islands, is covered by the 3D seismic data. The Bouguer gravity profile extracted along the seismic crossline 3,200 (Figure 12b) shows that the peak anomaly is about 170 mGal. At this location, filtered Bouguer gravity anomalies at high frequencies show two local maxima (Figures 9d–9f), related to the interpreted volcanic edifice and Brothers Islands, with the higher positive anomaly in correspondence with Brothers Islands where gabbros are exposed (Ligi et al., 2018, 2019). The seamount anomaly is found as an elongated oval shape toward NW-SE, while the shape of the anomaly at the Brothers Islands is an elongated oval shape toward the NE-SW (Figure 9f).

4.3. Analysis of Magnetic Anomalies

Magnetic anomalies of the NRS show values ranging between −100 and 200 nT (Figure 10). Most of the highest positive magnetic anomalies are found as spots along the axial trough and concentrated along the eastern coastline. The onshore areas show scattered and weak local positive anomalies (10–65 nT) corresponding to the Red Sea hills on the Egyptian side and Asir and Hijaz Mountains on the Arabian side and local occurrences of relatively lower anomalies (−5 to −80 nT). Nevertheless, the magnetic grid displays a low resolution, probably due to a lack of data in these areas (Figure 10a). A magnetic anomaly map for the study area was selected from the regional map of the NRS to highlight the magnetic pattern around the Brothers Islands (Figure 10b). This map, with contour lines 50 nT apart, displays values ranging from −120 to 170 nT. Five large-amplitude magnetic local maxima, aligned NE-SW, show values greater than 150 nT (Figure 10b). A RTP operator has been applied to minimize the polarity effects and center the anomalies directly above their source locations (Figure 10c). The RTP map shows that all the positive magnetic anomalies are shifted northward due to the removal of the dipolar effect of the Earth's magnetic field. The amplitude of the magnetic anomalies generally increases after RTP, and the magnetic gradients become steeper and more intensive.

Furthermore, after processing, a positive magnetic anomaly SW of the Brother Islands is observed, precisely in correspondence with a strong positive gravity anomaly. A magnetic profile along the track of crossline 3,200 shows values exceeding 170 nT in this location (Figure 12a). On the contrary, the basement high of the Brothers Islands itself shows no evidence for a local peak in the anomalies. Several magnetic highs can be observed in the RTP map, and they are characterized by high magnetic values of more than 150 nT and by a sub-circular shape. Four high-pass filtered maps with cutoffs of 10, 25, 50, and 100 km have been generated from the RTP map (Figure 11). The constructed figures displayed the same magnetic positive anomalies approximately on the exact location and similar shapes. Seven intense magnetic highs have been identified, with N-S, NW-SE, and NE-SW trending alignment (Figure 11).

5. Discussion

5.1. Evidences Supporting Recent Magmatism in Offshore Quseir

Combined observations from seismic, gravity, and magnetic data suggest that the seismic basement of the structural high southwest of the Brothers Islands displays some peculiarities regarding the nature of the underlying rocks. In particular (a) a positive magnetic anomaly precisely centered on the ridge summit and does not extend
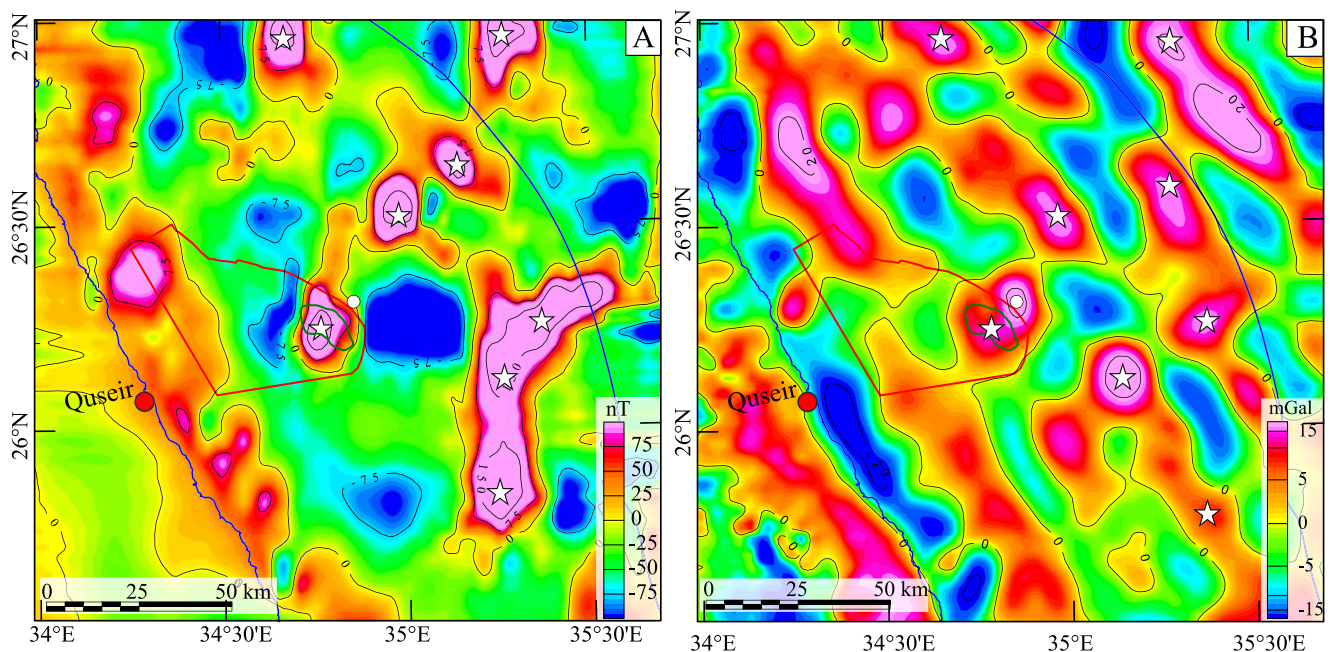
Figure 13. (a) Regional scale comparison between magnetic anomalies and (b) Bouguer gravity anomalies after high-pass filtering with cut-off wavelengths of 100 km. The two maps (approx. 175 × 175 km) show coincident, sub-circular localized anomalies outside the 3D seismic survey marked by a red polygon, interpreted as possible submarine volcanoes (white stars). The white dot locates the Brothers Islands.

over the neighboring Brothers high, indicating a high magnetization that probably a different lithology of the basement underlying the two structures, (b) the presence of a strong positive gravity anomaly SW of the Brothers Islands with gravity values up to 40 mGal, and (c) a marked difference in RMS reflection amplitudes from the surrounding and underlying rocks.

This leads to the hypothesis that the southwestern ridge is more recent than the Brothers Islands and has been formed by rapid ascent and cooling of basaltic magma, constraining its magnetization higher than that of the underlying basement and of the Brothers Islands high, where gabbros are exposed beneath the Pleistocene reef carapace of the islands (Bosworth et al., 1996; Ligi et al., 2018; Shukri, 1944; Taviani & Rabbi, 1984). In addition, its morphological shape, as observed in seismic sections, recalls an elliptical cone that culminates with two conical summits. These observations suggest that this ridge is a complex volcanic edifice developed on top of the seismic basement at 26°15'25" N; 34°46'53" E (datum WGS84). The buried portion of the volcanic apparatus is partly rooted in the basement and partly surrounded by halite and sedimentary rocks. In contrast, the submarine portion reaches a depth of 215 m and affects largely the seafloor morphology, which is compatible with recent extrusive activity (Figure 7f). Furthermore, its elongated structure may have been driven by the large rift-related extensional fault affecting its southwestern flank, favoring the ascent of melt.

The hypothesis of a submerged volcano was tested by forward modeling. The assumed geological model is 46 km long, 20 km deep, and includes the southwestern high (Figure 12c). The forward model was constructed using geometries deduced from the seismic data interpretation applying a narrow density value range of 2.7–2.82 g/cm^3 for the entire basement section and 2.65 g/cm^3 for the seamount above the basement with a high magnetic susceptibility value of 0.0034 cgs. The buried portion of the volcanic edifice is not precisely determined because of the difficulties in identifying its boundaries in contact with the basement. Nevertheless, the forward model shows a good match between the predicted and observed gravity and magnetic anomalies, with an error of 5.452 and 3.757 for the magnetic and gravity, respectively, supporting the volcanic origin of the seamount (Figures 12a and 12b).

Thus, the coexistence over the same area of physiographic-structural elements with high magnetic susceptibility and high density, inferred by magnetic and gravity anomalies, and associated with geological evidence from seismic data, strongly suggest the presence of a volcanic edifice. Adopting the same criteria, seven other similar volcanic seamounts outside of the 3D seismic coverage can be detected (Figure 13). These seamounts are developed probably due to the rapid ascent and cooling of basaltic magmas along a rifting-related fault during late

syn-rift times. However, without any information on their geometry and the nature of their basement, we can only affirm that they display similar geophysical signatures.

This interpretation provides new evidences for the recent magmatism in the western margin of the NRS from the interpretation of the 3D seismic survey as well supports and refines those of Cochran et al. (1986), Cochran (2005), Cochran and Karner (2007), Guennoc et al. (1988), and Martinez and Cochran (1988). They assumed that all the magnetic highs in the NRS are magnetic dipolar anomalies due to localized sources with normal magnetization, probably related to extrusive and intrusive bodies. Several authors suggest (Cochran, 2005; Cochran et al., 1986; Martinez & Cochran, 1988; Maury et al., 1985; Pautot et al., 1984) that they formed during the last 0.78 Ma (Pleistocene), after the last magnetic inversion, which is consistent with our observations. For the first time, this article provides a depth map and a 3D view for one of these recent volcanic edifices and discusses the changes in its shape and geometry laterally and vertically as well its relationships with the imaged seismic sequences.

5.2. Correlating Between Magmatism in Offshore Quseir and Western Arabia

Magmatism during the Cenozoic along the margins of the central and NRS rift systems has been abundant, particularly in western Arabia, where widespread volcanic fields form one of the largest alkali basalt provinces in the world (180,000 km², Chorowicz, 2005; Coleman et al., 1983; Moucha & Forte, 2011). Magmatism in this region (30 Ma–Present) preceded, was concurrent with, and continued after the Red Sea rift. Lava compositions in this province include tholeiites, but are predominantly basanite to alkali olivine basalt to hawaiite, with minor more evolved compositions (Altherr et al., 2019; Camp & Roobol, 1989, 1992; Camp et al., 1991; Coleman, 1993; Coleman et al., 1983; Duncan & Al-Amri, 2013; Moufti et al., 2012; Sanfilippo et al., 2019, 2021). Within several large centers, volcanic activity began (>12 Ma) with tholeiitic to transitional compositions, then became more alkaline for younger eruptions (<12 Ma) (Camp & Roobol, 1992). The older period of activity includes dikes and eruptive centers close to and aligned with the NW–SE Red Sea margin, while the younger volcanic centers are distributed over a 200 km swath and display N–S alignment. The most voluminous centers form a prominent N–S volcanic axis, the Makkah-Madinah-Nafud (MMN) line, where the volcanic activity occurred in pulses from 10 Ma up to the present day, with a progressive migration toward the north (Figure 14). The oldest MMN lava flows occurred in Harrat Rahat (about 10 Ma: Camp & Roobol, 1989). Further to the north, the oldest volcanic activity is dated at about 5 Ma in Harrat Khaybar, while in Harrat Ithnayn at 3 Ma (Camp et al., 1991). Recently, $^{40}Ar/^{39}Ar$ age determinations provided younger ages for the Harrat Ithnayn lavas ranging from 500 to 120 ka (Alhejji et al., 2019). This scenario seems compatible with a progressive rejuvenation of the magmatism at higher latitudes along the MMN line (Figure 14). Following the hypothesis of a northward rejuvenation of the volcanic products, we note that Harrat Ithnayn volcanic field rests at a comparable latitude with Quseir (26°N). We hypothesize that the magmatic events at similar latitudes along the Red Sea margins and with similar ages may have originated within the same geotectonic context. Most of the Cenozoic volcanic products of the *harrats* are related to alkaline and tholeiitic suites (e.g., Downs et al., 2019) and they have been interpreted to derive from different degrees of partial melting of a peridotitic source with poor crustal assimilation. The increased volcanic activity during the last 10 Ma has been interpreted as a response to a Western Arabian plate scale lithospheric up-doming, probably linked to a propagation of the Afar mantle plume toward the north (Camp & Roobol, 1992). In addition, the distribution of the volcanic vents along a NNW direction parallel to the Red Sea fault systems has been interpreted as a result of the reactivation of rift structures (Moufti et al., 2012, 2013).

The seamount object of the present study and the nearby possible equivalents can be considered in the framework of a regional-scale, late syn-rift magmatic reactivation of the structures along the margins. Although it is difficult, in the absence of geochemical and petrographic analyses from the studied sector, to propose a specific geodynamic scenario, a major change in the lithospheric setting must have occurred since 10 Ma. The studied example testifies that the effects of this event were not limited to the continental domain of the Arabian plate but extended further west, into the Red Sea and toward the African plate.

6. Conclusions

High magnetic susceptibility and high-density sub-circular areas centered on seafloor topographic highs characterize the NRS. One of these areas, to the southwest of Brothers Islands offshore Quseir, has been studied in detail using a 3D seismic data set that allows recognizing its architectural context, characterized by a rift-related normal
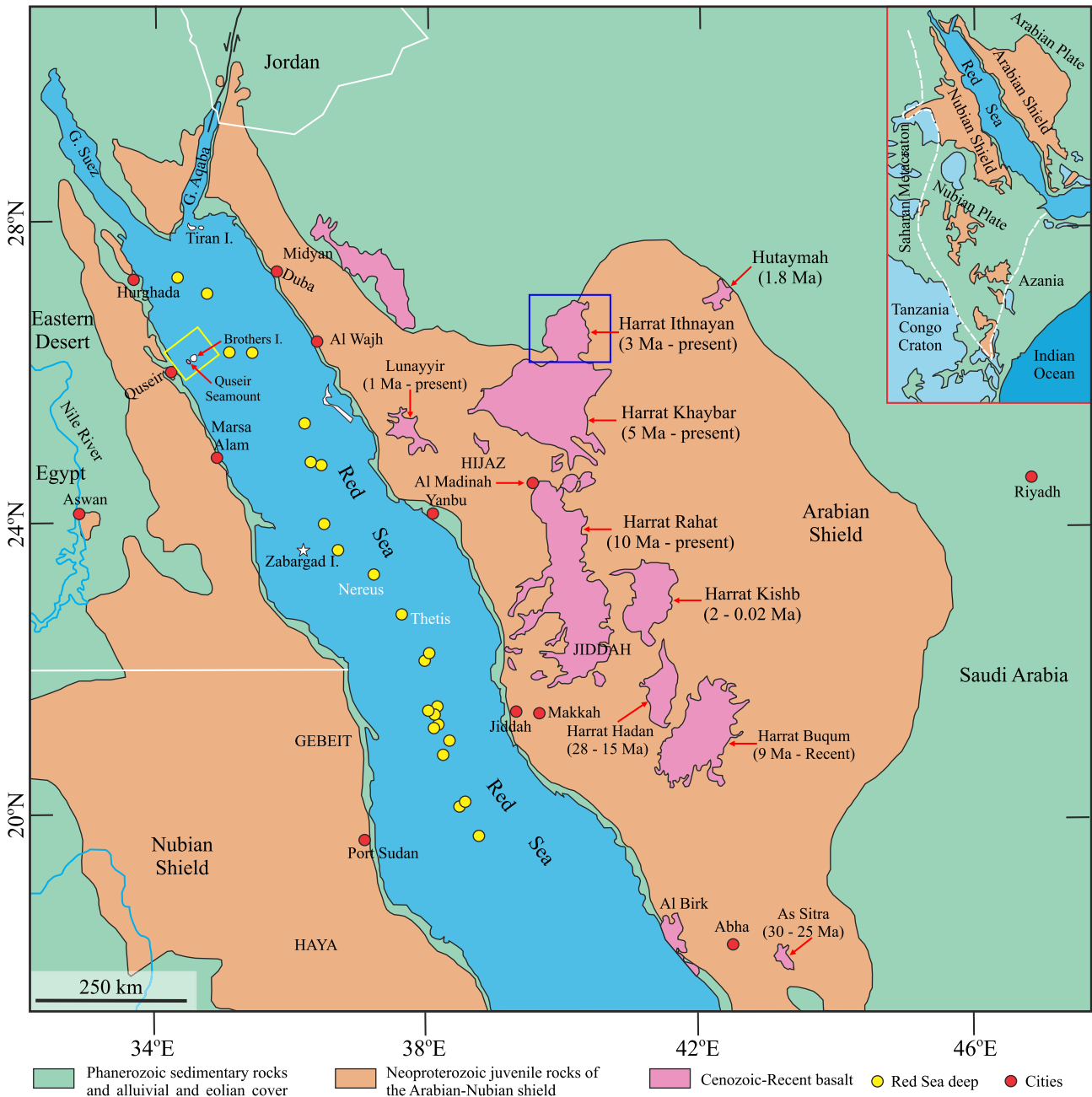
Figure 14. Regional map showing the volcanic regions (*Harrats*) and the northward rejuvenation of the volcanism in western Arabia. The yellow and blue boxes indicate the location of the studied recent seamount SW of the Brothers Islands and Harrat Ithnayn, respectively, modified from Coleman (1993) and Moufti et al. (2012).

fault and a prominent, shallow footwall-related basement high surrounded by syn-rift deposits. The basement high forms a pronounced physiographic body that rises from the surrounded seafloor by more than 520 m. The analysis of seismic amplitudes reveals that the structural high has a different seismic response when compared to the surrounding sedimentary sequence and the pre-rift basement. A forward model was calculated adopting the interpreted geological model and density and magnetization values compatible with a complex volcanic edifice on the summit of the basement high. The forward model shows good fitting between the measured and predicted Bouguer gravity and magnetic anomalies, suggesting a volcanic nature of the seamount located at 26°15'25" N and 34°46'53" E. Detailed observations based on 3D seismic interpretation allow us to define the shape and the volcanic edifice and the relationships with the imaged seismic sequences. Moreover, six classes of archi-

tectural features have been observed; dikes, sills, disrupted blocks, jacked-up domes, cone shaped morphology, and epiclastic plume. Our interpretation suggests that volcanic activity occurred at different centers forming a complex and composite edifice at the footwall of a large tilted block during late syn-rift and likely during Pleistocene. The same volcanic origin has been postulated for several additional neighboring areas having similar gravity and magnetic pattern, suggesting the presence of a cluster of volcanic edifices offshore Quseir. In addition, it is also suggested that the studied volcanic edifices can be compared with the volcanic fields of the western Arabian onshore, which formed, at a similar latitude, during the Pleistocene and were probably generated by the progressive northward migration of the Afar plume.

Data Availability Statement

Gridded satellite-derived free-air gravity anomaly data are available from https://topex.ucsd.edu/pub/global_grav_1min, the WGM2012 global gravity model (Bouguer anomalies) from https://bgi.obs-mip.fr/data-products/grids-and-models/wgm2012-global-model/, and the EMAG2$_{v3}$ earth magnetic anomaly grid is available from EMAG2v3: Earth Magnetic Anomaly Grid (2-arc-minute resolution) - catalog (data.gov). The seismic data were provided courtesy of BG Egypt (now Royal Dutch Shell) and images are published with the permission of South Valley Egyptian Petroleum Holding Company (Ganope).

References

Alhejji, S., Kent, A. J., Duncan, R. A., Graham, D. W., Al-Amri, A. M., & Alshaltoni, S. A. (2019). Geochronology and geochemistry of volcanism at Harrat Ithnayn, Western Saudi Arabia. *AGU Fall Meeting Abstracts*, *2019*, V11E–V0135.

Ali, M. (2020). Three-dimensional structural modelling and source rock evaluation of the Quseir Formation in the Komombo Basin, Egypt. *Acta Geologica Sinica-English Edition*, *94*(5), 1619–1634. https://doi.org/10.1111/1755-6724.14510

Ali, M., Abdelhady, A., Abdelmaksoud, A., Darwish, M., & Essa, M. A. (2020). 3D static modeling and petrographic aspects of the Albian/Cenomanian Reservoir, Komombo Basin, Upper Egypt. *Natural Resources Research*, *29*(2), 1259–1281. https://doi.org/10.1007/s11053-019-09521-5

Ali, M., Abdelmaksoud, A., Essa, M. A., Abdelhady, A., & Darwish, M. (2020). 3D structural, facies and petrophysical modeling of C member of six Hills formation, Komombo Basin, Upper Egypt. *Natural Resources Research*, *29*(4), 2575–2597. https://doi.org/10.1007/s11053-019-09583-5

Ali, M., Ali, M. Y., Abdelhady, A., & Fairhead, J. D. (2022). Tectonic evolution and subsidence history of the Cretaceous basins in southern Egypt: The Komombo Basin. *Basin Research*, *34*(5), 1731–1762. https://doi.org/10.1111/bre.12683

Ali, M., Darwish, M., Abdelhady, A., & Essa, M. A. (2017a). Case study of seismic interpretation in Al Baraka Oil field, Komombo Basin, Upper Egypt. In *The Fifth International Conference for Young Scientist in Basic and Applied Science*.

Ali, M., Darwish, M., Abdelhady, A., & Essa, M. A. (2017b). Structural and lithostratigraphic evolution of Al Baraka Oil field, Komombo Basin, Upper Egypt as deduce from 2D seismic lines and well logging data. *Journal of Basic and Environmental Sciences*, *2*, 149–169.

Ali, M., Darwish, M., Essa, M. A., & Abdelhady, A. (2018). 2D seismic interpretation and characterization of the Hauterivian–Early Barremian source rock in Al Baraka oil field, Komombo Basin, Upper Egypt. *Journal of African Earth Sciences*, *139*, 113–119. https://doi.org/10.1016/j.jafrearsci.2017.12.010

Ali, M., Darwish, M., Essa, M. A., & Abdelhady, A. (2019). Comparison between source rock potential of the Dakhla Formation in Komombo Basin and Gebel Duwi, Upper Egypt. *Arabian Journal of Geosciences*, *12*(19), 613. https://doi.org/10.1007/s12517-019-4833-y

Ali, M., Decarlis, A., Ceriani, A., & Ligi, M. (2021). Rifting dynamics and margin architecture in northern Red Sea, Egypt. In *UAE Graduate Students Research Conference* (pp. 1–2).

Ali, M., Ligi, M., Ceriani, A., Bouchaala, F., Bosworth, W., & Decarlis, A. (2022). Birth of a large Quaternary volcanic edifice southwest of the Brothers islets, northern Red Sea, Egyptian Margin. In *Working Group on Mediterranean Ophiolites Conference, Abstracts* (Vol. *1*).

Almalki, K. A., Betts, P. G., & Ailleres, L. (2014). Episodic seafloor spreading in the southern Red Sea. *Tectonophysics*, *617*, 140–149. https://doi.org/10.1016/j.tecto.2014.01.030

Altherr, R., Mertz-Kraus, R., Volker, F., Kreuzer, H., Henjes-Kunst, F., & Lange, U. (2019). Geodynamic setting of upper Miocene to Quaternary alkaline basalts from Harrat al 'Uwayrid (NW Saudi Arabia): Constraints from K Ar dating, chemical and Sr-Nd-Pb isotope compositions, and petrological modeling. *Lithos*, *330*, 120–138. https://doi.org/10.1016/j.lithos.2019.02.007

Augustin, N., Devey, C. W., & van der Zwan, F. M. (2019). A modern view on the red sea rift: Tectonics, volcanism, and salt blankets. In *Geological Setting, Palaeoenvironment and Archaeology of the Red Sea* (pp. 37–52). Springer.

Augustin, N., Van der Zwan, F. M., Devey, C. W., & Brandsdóttir, B. (2021). 13 million years of seafloor spreading throughout the Red Sea Basin. *Nature Communications*, *12*(1), 1–10. https://doi.org/10.1038/s41467-021-22586-2

Ball, P. J., Stockli, D. F., Robbins, S., Tugend, J., & Masini, E. (2018). Northern Red Sea: Unravelling the tectono-thermal evolution of a hyper-extended rift system. *La Réunion Des Sciences de La Terre, Abstract*, *26*, 245.

Balmino, G., Vales, N., Bonvalot, S., & Briais, A. (2012). Spherical harmonic modelling to ultra-high degree of Bouguer and isostatic anomalies. *Journal of Geodesy*, *86*(7), 499–520. https://doi.org/10.1007/s00190-011-0533-4

Barakat, H., & Miller, P. (1984). Geology and petroleum exploration, Safaga concession, northern Red Sea, Egypt. In *Proceedings of the 7th Exploration Seminar* (pp. 191–214). Egyptian General Petroleum Corporation.

Ben-Avraham, Z. (1985). Structural framework of the gulf of Elat (Aqaba), northern Red Sea. *Journal of Geophysical Research*, *90*(B1), 703–726. https://doi.org/10.1029/jb090ib01p00703

Bischoff, A., Nicol, A., Cole, J., & Gravley, D. D. (2019). Stratigraphy of architectural elements of a buried monogenetic volcanic system and implications for geoenergy exploration.

Bojar, A.-V., Fritz, H., Kargl, S., & Unzog, W. (2002). Phanerozoic tectonothermal history of the Arabian–Nubian shield in the Eastern Desert of Egypt: Evidence from fission track and paleostress data. *Journal of African Earth Sciences*, *34*(3–4), 191–202. https://doi.org/10.1016/s0899-5362(02)00018-0

Bonatti, E., Cipriani, A., & Lupi, L. (2015). The Red Sea: Birth of an Ocean. In *The Red Sea* (pp. 29–44). Springer.

Bonatti, E., & Seyler, M. (1987). Crustal underplating and evolution in the Red Sea rift: Uplifted gabbro/gneiss crustal complexes on Zabargad and Brothers Islands. *Journal of Geophysical Research*, *92*(B12), 12803–12821. https://doi.org/10.1029/jb092ib12p12803

Bonvalot, S., Balmino, G., Briais, A., Kuhn, M., Peyrefitte, A., Vales, N., et al. (2012). World gravity map. *Commission for the Geological Map of the World*.

Bosworth, W. (1994). A model for the three-dimensional evolution of continental rift basins, north-east Africa. *Geologische Rundschau*, *83*(4), 671–688. https://doi.org/10.1007/bf00251067

Bosworth, W. (2015). Geological evolution of the Red Sea: Historical background, review, and synthesis. In *The Red Sea* (pp. 45–78). Springer.

Bosworth, W., & Burke, K. (2005). Evolution of the Red Sea—Gulf of Aden rift system. *Petroleum Systems of Divergent Continental Margin Basins*, 342–372.

Bosworth, W., Crevello, P., Winn, R. D., & Steinmetz, J. (1998). Structure, sedimentation, and basin dynamics during rifting of the Gulf of Suez and north-western Red Sea. In *Sedimentation and Tectonics in Rift Basins Red Sea:-Gulf of Aden* (pp. 77–96). Springer.

Bosworth, W., Darwish, M., Crevello, P., Taviani, M., & Marshak, S. (1996). Stratigraphic and structural evolution of Zabargad island (Red Sea, Egypt) since the early Cretaceous. *Proceedings of the 3rd International Conference on Geology of the Arab World*, *1*, 161–190.

Bosworth, W., Huchon, P., & McClay, K. (2005). The red sea and gulf of aden basins. *Journal of African Earth Sciences*, *43*(1–3), 334–378. https://doi.org/10.1016/j.jafrearsci.2005.07.020

Bosworth, W., Khalil, S. M., Ligi, M., Stockli, D. F., & McClay, K. R. (2020). Geology of Egypt: The northern Red Sea. In *The Geology of Egypt* (pp. 343–374). Springer.

Bosworth, W., & McClay, K. (2001). Structural and stratigraphic evolution of the Gulf of Suez rift, Egypt: A synthesis. *Mémoires Du Muséum National d'histoire Naturelle (1993)*, *186*, 567–606.

Bosworth, W., Montagna, P., Pons-Branchu, E., Rasul, N., & Taviani, M. (2017). Seismic hazards implications of uplifted Pleistocene coral terraces in the Gulf of Aqaba. *Scientific Reports*, *7*(1), 1–13. https://doi.org/10.1038/s41598-017-00074-2

Bosworth, W., & Stockli, D. F. (2016). Early magmatism in the greater Red Sea rift: Timing and significance. *Canadian Journal of Earth Sciences*, *53*(11), 1158–1176. https://doi.org/10.1139/cjes-2016-0019

Bosworth, W., Sultan, M., Stern, R. J., Arvidson, R. E., Shore, P., & Becker, R. (1993). Nature of the Red Sea crust: A controversy revisited: Comment and reply. *Geology*, *21*(6), 574–576. https://doi.org/10.1130/0091-7613(1993)021<0574:notrsc>2.3.co;2

Camp, V. E., & Roobol, M. J. (1989). The Arabian continental alkali basalt province: Part I. Evolution of Harrat Rahat, Kingdom of Saudi Arabia. *The Geological Society of America Bulletin*, *101*(1), 71–95. https://doi.org/10.1130/0016-7606(1989)101<0071:tacabp>2.3.co;2

Camp, V. E., & Roobol, M. J. (1992). Upwelling asthenosphere beneath western Arabia and its regional implications. *Journal of Geophysical Research*, *97*(B11), 15255–15271. https://doi.org/10.1029/92jb00943

Camp, V. E., Roobol, M. J., & Hooper, P. R. (1991). The Arabian continental alkali basalt province: Part II. Evolution of Harrats Khaybar, Ithnayn, and Kura, Kingdom of Saudi Arabia. *The Geological Society of America Bulletin*, *103*(3), 363–391. https://doi.org/10.1130/0016-7606(1991)103<0363:tacabp>2.3.co;2

Chorowicz, J. (2005). The east African rift system. *Journal of African Earth Sciences*, *43*(1–3), 379–410. https://doi.org/10.1016/j.jafrearsci.2005.07.019

Cochran, J. R. (1983). A model for development of Red Sea. *AAPG Bulletin*, *67*(1), 41–69.

Cochran, J. R. (2005). Northern Red Sea: Nucleation of an oceanic spreading center within a continental rift. *Geochemistry, Geophysics, Geosystems*, *6*(3). https://doi.org/10.1029/2004gc000826

Cochran, J. R., Gaulier, J. M., & Le Pichon, X. (1991). Crustal structure and the mechanism of extension in the northern Red Sea: Constraints from gravity anomalies. *Tectonics*, *10*(5), 1018–1037. https://doi.org/10.1029/91tc00926

Cochran, J. R., & Karner, G. D. (2007). Constraints on the deformation and rupturing of continental lithosphere of the Red Sea: The transition from rifting to drifting. *Geological Society, London, Special Publications*, *282*(1), 265–289. https://doi.org/10.1144/sp282.13

Cochran, J. R., Martinez, F., Steckler, M. S., & Hobart, M. A. (1986). Conrad deep: A new northern Red Sea deep: Origin and implications for continental rifting. *Earth and Planetary Science Letters*, *78*(1), 18–32. https://doi.org/10.1016/0012-821x(86)90169-x

Coleman, R. G. (1993). Geological evolution of the Red Sea. In *Oxford Monographs on Geology and Geophysics* (Vol. 24, p. 186). Oxford University Press.

Coleman, R. G., Gregory, R. T., & Brown, G. F. (1983). Cenozoic volcanic rocks of Saudi Arabia. Saudi Arabian. *Deputy Minister of Mineral Resources*, Open File Report USGS-OF-03-93.

Cooper, G. R. J., & Cowan, D. R. (2005). Differential reduction to the pole. *Computers & Geosciences*, *31*(8), 989–999. https://doi.org/10.1016/j.cageo.2005.02.005

Downs, D. T., Robinson, J. E., Stelten, M. E., Champion, D. E., Dietterich, H. R., Sisson, T. W., et al. (2019). *Geologic map of the northern Harrat Rahat volcanic field, Kingdom of Saudi Arabia*. US Department of the Interior.

Duncan, R. A., & Al-Amri, A. M. (2013). Timing and composition of volcanic activity at Harrat Lunayyir, western Saudi Arabia. *Journal of Volcanology and Geothermal Research*, *260*, 103–116. https://doi.org/10.1016/j.jvolgeores.2013.05.006

Ehrhardt, A., Hübscher, C., Ben-Avraham, Z., & Gajewski, D. (2005). Seismic study of pull-apart-induced sedimentation and deformation in the northern Gulf of Aqaba (Elat). *Tectonophysics*, *396*(1–2), 59–79. https://doi.org/10.1016/j.tecto.2004.10.011

Gettings, M. E., Blank, H. R., Jr., Mooney, W. D., & Healey, J. H. (1986). Crustal structure of southwestern Saudi Arabia. *Journal of Geophysical Research*, *91*(B6), 6491–6512. https://doi.org/10.1029/jb091ib06p06491

Girdler, R. W. (1990). The Dead Sea transform fault system. *Tectonophysics*, *180*(1), 1–13. https://doi.org/10.1016/0040-1951(90)90367-h

Girdler, R. W., & Whitmarsh, R. (1974). Miocene Evaporites in Red Sea cores, their relevance to the problem of the width and age of oceanic crust beneath the Red Sea.

Gordon, G., Hansen, B., Scott, J., Hirst, C., Graham, R., Grow, T., et al. (2010). The hydrocarbon prospectivity of the Egyptian North Red Sea basin. *Geological Society, London, Petroleum Geology Conference Series*, *7*(1), 783–789. https://doi.org/10.1144/0070783

Guennoc, P., Pautot, G., & Coutelle, A. (1988). Surficial structures of the northern Red Sea axial valley from 23 N to 28 N: Time and space evolution of neo-oceanic structures. *Tectonophysics*, *153*(1–4), 1–23. https://doi.org/10.1016/0040-1951(88)90005-4

Holford, S., Schofield, N., MacDonald, J., Duddy, I., & Green, P. (2012). Seismic analysis of igneous systems in sedimentary basins and their impacts on hydrocarbon prospectivity: Examples from the southern Australian margin. *The APPEA Journal*, *52*(1), 229–252. https://doi.org/10.1071/aj11017

Hughes, G. W., & Beydoun, Z. R. (1992). The Red Sea—Gulf of Aden: Biostratigraphy, lithostratigraphy and palaeoenvironments. *Journal of Petroleum Geology*, *15*(s3), 135–156. https://doi.org/10.1111/j.1747-5457.1992.tb00959.x

Hughes, G. W., Perincek, D., Abu-Bshait, A. J., & Jarad, A. R. M. (2000). Aspects of Midyan geology, Saudi Arabian Red Sea. *Saudi Aramco Journal of Technology*, *1999*, 12–42.

Hughes, G. W. A. G., & Johnson, R. S. (2005). Lithostratigraphy of the Red Sea region. *GeoArabia*, *10*(3), 49–126. https://doi.org/10.2113/geoarabia100349

Izzeldin, A. Y. (1987). Seismic, gravity and magnetic surveys in the central part of the Red Sea: Their interpretation and implications for the structure and evolution of the Red Sea. *Tectonophysics*, *143*(4), 269–306. https://doi.org/10.1016/0040-1951(87)90214-9

Jarrige, J., Ott d'Estevou, P., Burollet, P. F., Montenat, C., Prat, P., Richert, J., & Thiriet, J. (1990). The multistage tectonic evolution of the Gulf of Suez and northern Red Sea continental rift from field observations. *Tectonics*, *9*(3), 441–465. https://doi.org/10.1029/tc009i003p00441

Johnson, P. R. (2014). An expanding Arabian-Nubian shield geochronologic and isotopic dataset: Defining limits and confirming the tectonic setting of a Neoproterozoic accretionary orogen. *The Open Geology Journal*, *8*(1), 3–33. https://doi.org/10.2174/1874262901408010003

Jones, D. A., Wilson, G. S., Gorman, A. R., Fox, B. R. S., Lee, D. E., & Kaulfuss, U. (2017). A drill-hole calibrated geophysical characterisation of the 23 Ma Foulden Maar stratigraphic sequence, Otago, New Zealand. *New Zealand Journal of Geology and Geophysics*, *60*(4), 465–477. https://doi.org/10.1080/00288306.2017.1369130

Keating, P., & Zerbo, L. (1996). An improved technique for reduction to the pole at low latitudes. *Geophysics*, *61*(1), 131–137. https://doi.org/10.1190/1.1443933

Khalil, S. M., & McClay, K. R. (2001). Tectonic evolution of the NW Red Sea-Gulf of Suez rift system. *Geological Society, London, Special Publications*, *187*(1), 453–473. https://doi.org/10.1144/gsl.sp.2001.187.01.22

Khalil, S. M., & McClay, K. R. (2009). Structural control on syn-rift sedimentation, northwestern Red Sea margin, Egypt. *Marine and Petroleum Geology*, *26*(6), 1018–1034. https://doi.org/10.1016/j.marpetgeo.2008.09.001

Khalil, S. M., & McClay, K. R. (2017). 3D geometry and kinematic evolution of extensional fault-related folds, NW Red Sea, Egypt. *Geological Society, London, Special Publications*, *439*(1), 109–130. https://doi.org/10.1144/sp439.11

Khalil, S. M., & McClay, K. R. (2020). Extensional fault-Related folding in the northwestern Red Sea, Egypt: Segmented fault growth, fault linkages, corner folds and basin evolution. *Geological Society, London, Special Publications*, *476*(1), 49–81. https://doi.org/10.1144/sp476.12

Le Magoarou, C., Hirsch, K., Fleury, C., Martin, R., Ramirez-Bernal, J., & Ball, P. (2021). Integration of gravity, magnetic, and seismic data for subsalt modeling in the Northern Red Sea. *Interpretation*, *9*(2), T507–T521. https://doi.org/10.1190/int-2019-0232.1

Li, X. (2008). Magnetic reduction-to-the-pole at low latitudes: Observations and considerations. *The Leading Edge*, *27*(8), 990–1002. https://doi.org/10.1190/1.2967550

Ligi, M., Bonatti, E., Bosworth, W., Cai, Y., Cipriani, A., Palmiotto, C., et al. (2018). Birth of an ocean in the Red Sea: Oceanic-type basaltic melt intrusions precede continental rupture. *Gondwana Research*, *54*, 150–160. https://doi.org/10.1016/j.gr.2017.11.002

Ligi, M., Bonatti, E., Bosworth, W., & Ronca, S. (2019). Oceanization starts at depth during continental rupturing in the northern Red Sea. In *Geological Setting, Palaeoenvironment and Archaeology of the Red Sea* (pp. 131–157). Springer.

Lorenz, V., & Kurszlaukis, S. (2007). Root zone processes in the phreatomagmatic pipe emplacement model and consequences for the evolution of maar–diatreme volcanoes. *Journal of Volcanology and Geothermal Research*, *159*(1–3), 4–32. https://doi.org/10.1016/j.jvolgeores.2006.06.019

Makris, J., & Rihm, R. (1991). Shear-controlled evolution of the Red Sea: Pull apart model. *Tectonophysics*, *198*(2–4), 441–466.

Martinez, F., & Cochran, J. R. (1988). Structure and tectonics of the northern Red Sea: Catching a continental margin between rifting and drifting. *Tectonophysics*, *150*(1–2), 1–31. https://doi.org/10.1016/0040-1951(88)90293-4

Maury, R. C., Bougault, H., Coutelle, A., Guennoc, P., & Joron, J.-L. (1985). Présence de ferrobasalte tholéititique dans la fosse Jean-Charcot (26° 15'N, 35° 22'E): Signification dans le contexte géodynamique de la Mer Rouge. *Comptes Rendus de l'Académie Des Sciences. Série 2, Mécanique, Physique, Chimie, Sciences de l'univers, Sciences de La Terre*, *300*(16), 811–816.

McLean, C. E., Schofield, N., Brown, D. J., Jolley, D. W., & Reid, A. (2017). 3D seismic imaging of the shallow plumbing system beneath the Ben Nevis Monogenetic volcanic field: Faroe–Shetland Basin. *Journal of the Geological Society*, *174*(3), 468–485. https://doi.org/10.1144/jgs2016-118

Meyer, B., Saltus, R., & Chulliat, A. (2017). EMAG2 Version 3-Update of a two arc-minute global magnetic anomaly grid. *EGU General Assembly Conference Abstracts*, 10614.

Miller, P. M., & Barakat, H. (1988). Geology of the safaga concession, northern Red Sea, Egypt. *Tectonophysics*, *153*(1–4), 123–136. https://doi.org/10.1016/0040-1951(88)90010-8

Mitchell, N. C. (2001). Transition from circular to stellate forms of submarine volcanoes. *Journal of Geophysical Research*, *106*(B2), 1987–2003. https://doi.org/10.1029/2000jb900263

Mitchell, N. C., Ligi, M., Feldens, P., & Hübscher, C. (2017). Deformation of a young salt giant: Regional topography of the R ed S ea M iocene evaporites. *Basin Research*, *29*, 352–369. https://doi.org/10.1111/bre.12153

Mitchell, N. C., Ligi, M., Ferrante, V., Bonatti, E., & Rutter, E. (2010). Submarine salt flows in the central Red Sea. *Bulletin*, *122*(5–6), 701–713. https://doi.org/10.1130/b26518.1

Mitchell, N. C., Ligi, M., & Rasul, N. M. A. (2019). Variations in Plio-Pleistocene deposition in the Red Sea. In *Geological Setting, Palaeoenvironment and Archaeology of the Red Sea* (pp. 323–339). Springer.

Montenat, C., D'Estevou, P. O., Purser, B., Burollet, P.-F., Jarrige, J.-J., Orszag-Sperber, F., et al. (1988). Tectonic and sedimentary evolution of the Gulf of Suez and the northwestern Red Sea. *Tectonophysics*, *153*(1–4), 161–177. https://doi.org/10.1016/0040-1951(88)90013-3

Moucha, R., & Forte, A. M. (2011). Changes in African topography driven by mantle convection. *Nature Geoscience*, *4*(10), 707–712. https://doi.org/10.1038/ngeo1235

Moufti, M. R., Moghazi, A. M., & Ali, K. A. (2012). Geochemistry and Sr–Nd–Pb isotopic composition of the Harrat Al-Madinah volcanic field, Saudi Arabia. *Gondwana Research*, *21*(2–3), 670–689. https://doi.org/10.1016/j.gr.2011.06.003

Moufti, M. R., Moghazi, A. M., & Ali, K. A. (2013). 40Ar/39Ar geochronology of the Neogene-Quaternary Harrat Al-Madinah intercontinental volcanic field, Saudi Arabia: Implications for duration and migration of volcanic activity. *Journal of Asian Earth Sciences*, *62*, 253–268. https://doi.org/10.1016/j.jseaes.2012.09.027

Mougenot, D., & Al-Shakhis, A. A. (1999). Depth imaging sub-salt structures: A case study in the Midyan Peninsula (Red Sea). *GeoArabia*, *4*(4), 445–464. https://doi.org/10.2113/geoarabia0404445

Moustafa, A. R., & Khalil, S. M. (2017). Control of compressional transfer zones on syntectonic and post-tectonic sedimentation: Implications for hydrocarbon exploration. *Journal of the Geological Society*, *174*(2), 336–352. https://doi.org/10.1144/jgs2016-030

Moustafa, A. R., & Khalil, S. M. (2020). Structural setting and tectonic evolution of the Gulf of Suez, NW Red Sea and Gulf of Aqaba Rift Systems. In *The Geology of Egypt* (pp. 295–342). Springer.

Muirhead, J. D., Van Eaton, A. R., Re, G., White, J. D. L., & Ort, M. H. (2016). Monogenetic volcanoes fed by interconnected dikes and sills in the Hopi Buttes volcanic field, Navajo Nation, USA. *Bulletin of Volcanology*, *78*(2), 11. https://doi.org/10.1007/s00445-016-1005-8

Omar, G. I., & Steckler, M. S. (1995). Fission track evidence on the initial rifting of the Red Sea: Two pulses, no propagation. *Science*, *270*(5240), 1341–1344. https://doi.org/10.1126/science.270.5240.1341

Patton, T. L., Moustafa, A. R., Nelson, R. A., & Abdine, S. A. (1994). Tectonic evolution and structural setting of the Suez rift: Chapter 1: Part I. *Type Basin: Gulf of Suez*.

Pautot, G., Guennoc, P., Coutelle, A., & Lyberis, N. (1984). Discovery of a large brine deep in the northern Red Sea. *Nature*, *310*(5973), 133–136. https://doi.org/10.1038/310133a0

Planke, S., Rasmussen, T., Rey, S. S., & Myklebust, R. (2005). Seismic characteristics and distribution of volcanic intrusions and hydrothermal vent complexes in the Vøring and Møre basins. *Geological Society, London, Petroleum Geology Conference Series*, *6*(1), 833–844. https://doi.org/10.1144/0060833

Quennell, A. M. (1951). *The geology and mineral resources of (former) Trans-Jordan*. HM Stationery Office.

Quennell, A. M. (1958). The structural and geomorphic evolution of the Dead Sea Rift. *Quarterly Journal of the Geological Society*, *114*(1–4), 1–24. https://doi.org/10.1144/gsjgs.114.1.0001

Rogers, J. J. W., Ghuma, M. A., Nagy, R. M., Greenberg, J. K., & Fullagar, P. D. (1978). Plutonism in Pan-African belts and the geologic evolution of northeastern Africa. *Earth and Planetary Science Letters*, *39*(1), 109–117. https://doi.org/10.1016/0012-821x(78)90147-4

Ross, D. A., & Schlee, J. (1973). Shallow structure and geologic development of the southern Red Sea. *The Geological Society of America Bulletin*, *84*(12), 3827–3848. https://doi.org/10.1130/0016-7606(1973)84<3827:ssagdo>2.0.co;2

Rowan, M. G. (2014). Passive-margin salt basins: Hyperextension, evaporite deposition, and salt tectonics. *Basin Research*, *26*(1), 154–182. https://doi.org/10.1111/bre.12043

Said, R. (1990). Quaternary. *The Geology of Egypt*, 487–510. https://doi.org/10.1201/9780203736678-25

Saleh, S., Jahr, T., Jentzsch, G., Saleh, A., & Abou Ashour, N. M. (2006). Crustal evaluation of the northern Red Sea rift and Gulf of Suez, Egypt from geophysical data: 3-dimensional modeling. *Journal of African Earth Sciences*, *45*(3), 257–278. https://doi.org/10.1016/j.jafrearsci.2006.02.001

Salem, A., Green, C., Campbell, S., Fairhead, J. D., Cascone, L., & Moorhead, L. (2013). Moho depth and sediment thickness estimation beneath the Red Sea derived from satellite and terrestrial gravity data. *Geophysics*, *78*(5), G89–G101. https://doi.org/10.1190/geo2012-0150.1

Sandwell, D. T., Müller, R. D., Smith, W. H. F., Garcia, E., & Francis, R. (2014). New global marine gravity model from CryoSat-2 and Jason-1 reveals buried tectonic structure. *Science*, *346*(6205), 65–67. https://doi.org/10.1126/science.1258213

Sanfilippo, A., Jácome, A. P. G., & Ligi, M. (2019). Geochemistry of the lunayyir and khaybar volcanic fields (Saudi Arabia): Insights into the origin of cenozoic Arabian volcanism. In *Geological Setting, Palaeoenvironment and Archaeology of the Red Sea* (pp. 389–415). Springer.

Sanfilippo, A., Sani, C., Rasul, N., Stewart, I. C. F., Vigliotti, L., Widinly, N., et al. (2021). Hidden but Ubiquitous: The Pre-Rift Continental Mantle in the Red Sea region. *Frontiers of Earth Science*, *666*. https://doi.org/10.3389/feart.2021.699460

Senger, K., Millett, J., Planke, S., Ogata, K., Eide, C. H., Festøy, M., et al. (2017). Effects of igneous intrusions on the petroleum system: A review. *First Break*, *35*(6). https://doi.org/10.3997/1365-2397.2017011

Shi, W., Mitchell, N. C., Kalnins, L. M., & Izzeldin, A. Y. (2018). Oceanic-like axial crustal high in the central Red Sea. *Tectonophysics*, *747*, 327–342. https://doi.org/10.1016/j.tecto.2018.10.011

Shukri, N. M. (1944). On the geology of the Brothers islets-northern Red Sea. *Bulletin of the Faculty of Science Cairo University*, *25*, 175–196.

Stern, R. J., Gottfried, D., & Hedge, C. E. (1984). Late Precambrian rifting and crustal evolution in the northeastern Desert of Egypt. *Geology*, *12*(3), 168–172. https://doi.org/10.1130/0091-7613(1984)12<168:lprace>2.0.co;2

Stockli, D. F., & Bosworth, W. (2019). Timing of extensional faulting along the magma-poor central and northern Red Sea rift margin—Transition from regional extension to necking along a hyperextended rifted margin. In *Geological Setting, Palaeoenvironment and Archaeology of the Red Sea* (pp. 81–111). Springer.

Taviani, M., Bonatti, E., Colantoni, P., & Rossi, P. L. (1986). Tectonically uplifted crustal blocks in the northern Red Sea: Data from the Brothers islets. *Memorie della Societa Geologica Italiana*, *27*(1984), 47–50.

Taviani, M., & Rabbi, E. (1984). Marine botryoidal aragonite in Pleistocene reef limestones of Red Sea offshore islands (northern Brother and Rocky island). *Mineralogica et Petrographica Acta*, *28*, 49–58.

Tewfik, N., & Ayyad, M. (1982). Petroleum exploration in the Red Sea shelf of Egypt. Proc. *6th Exploration Seminar, Egyptian General Petroleum Corporation and Egypt Petroleum Exploration Society, Cairo*, *1*, 159–180.

White, J. D. L., & Ross, P.-S. (2011). Maar-diatreme volcanoes: A review. *Journal of Volcanology and Geothermal Research*, *201*(1–4), 1–29. https://doi.org/10.1016/j.jvolgeores.2011.01.010